Pulsational Pair-instability Supernovae in Very Close Binaries

Pablo Marchant ¹, Mathieu Renzo^{2,3}, Robert Farmer^{2,3}, Kaliroe M. W. Pappas ⁴, Ronald E. Taam ¹, Selma E. de Mink^{2,3}, and Vassiliki Kalogera ¹

¹ Center for Interdisciplinary Exploration and Research in Astrophysics (CIERA) and Department of Physics and Astronomy, Northwestern University, 2145 Sheridan Road, Evanston, IL 60208, USA; pablo.marchant@northwestern.edu

Anton Pannenkoek Institute for Astronomy, University of Amsterdam, NL-1090 GE Amsterdam, The Netherlands
 ³ GRAPPA, University of Amsterdam, Science Park 904, 1098 XH Amsterdam, The Netherlands
 ⁴ Department of Physics, University of Illinois at Urbana-Champaign, 1110 W. Green St., Loomis Laboratory, Urbana, IL 61801, USA
 Received 2018 October 31; revised 2019 July 8; accepted 2019 July 21; published 2019 August 30

Abstract

Pair-instability and pulsational pair-instability supernovae (PPISNe) have not been unambiguously observed so far. They are, however, promising candidates for the progenitors of the heaviest binary black hole (BBH) mergers detected. If these BBHs are the product of binary evolution, then PPISNe could occur in very close binaries. Motivated by this, we discuss the implications of a PPISN happening with a close binary companion and what impact these events have on the formation of merging BBHs through binary evolution. For this, we have computed a set of models of metal-poor ($Z_{\odot}/10$) single helium stars using the MESA software instrument. For PPISN progenitors with pre-pulse masses $>50\,M_{\odot}$ we find that, after a pulse, heat deposited throughout the layers of the star that remain bound causes it to expand to more than $100\,R_{\odot}$ for periods of 10^2-10^4 yr depending on the mass of the progenitor. This results in long-lived phases of Roche lobe overflow or even common-envelope events if there is a close binary companion, leading to additional electromagnetic transients associated with PPISN eruptions. If we ignore the effect of these interactions, we find that mass loss from PPISNe reduces the final BH spin by $\sim 30\%$, induces eccentricities below the threshold of detectability of the LISA observatory, and can produce a double-peaked distribution of measured chirp masses in BBH mergers observed by ground-based detectors.

Key words: binaries: close - stars: black holes - stars: massive - supernovae: general

1. Introduction

The production of electron–positron pairs in the cores of very massive stars has long been proposed to cause their collapse before oxygen is depleted in their cores, leading to a thermonuclear explosion (Fowler & Hoyle 1964; Rakavy & Shaviv 1967). Stars with helium cores in the range of $M_{\rm He} \sim 60\text{--}130\,M_{\odot}$ (corresponding to zero-age main-sequence masses between \sim 140 and $260\,M_{\odot}$ for nonrotating stars without mass loss) are expected to be completely disrupted by this event, with the higher-mass progenitors possibly being observable as superluminous supernovae (SNe) owing to nickel yields of up to tens of solar masses (Heger & Woosley 2002). Less massive stars, with helium core masses in the range of $M_{\rm He} \sim 30{\text -}60\,M_{\odot}$ (zero-age mainsequence masses $\sim 70-140 \, M_{\odot}$), are also expected to become unstable but produce instead a series of energetic pulses and mass ejections before finally collapsing to a black hole (BH; Fraley 1968; Woosley 2017). These two types of events are referred to as pairinstability SNe (PISNe) and pulsational pair-instability SNe (PPISNe), respectively. Stars with cores in excess of $M_{\rm He} \sim$ $130\,M_{\odot}$ are also predicted to become unstable, but energy losses due to photodisintegration of heavy elements prevent a thermonuclear explosion and allow the formation of a BH (Bond et al. 1982; Woosley & Weaver 1982; Heger & Woosley 2002). Although no observed SN has been conclusively identified to be either a PISN or a PPISN, theoretical models consistently predict these transients, with physical uncertainties such as rotation (Chatzopoulos & Wheeler 2012) or nuclear reaction rates (Takahashi 2018) only shifting the mass ranges listed above.

Various potential candidate events from hydrogen-rich SNe have been observed. OGLE-2014-SN-073 is one such PISN candidate, with a derived ejecta mass of $60^{+45}_{-16}\,M_{\odot}$ and a nickel mass $>0.47\pm0.02\,M_{\odot}$ (Terreran et al. 2017). SN 2006gy, on

the other hand, has been proposed to be powered by the collision of ejected shells in a PPISN (Woosley et al. 2007). This is also the case for iPTF14hls, as its light curve exhibits multiple peaks and a high brightness for more than 600 days (Arcavi et al. 2017; see Woosley 2018 for a discussion on potential progenitors). Regarding hydrogen-poor events, the Type I superluminous SN SN 2007bi has been suggested to be the product of a PISN with a nickel yield $>3 M_{\odot}$ (Gal-Yam et al. 2009). Another Type I superluminous event, iPTF16eh, produced a light echo on a shell of material ejected ~32 yr prior to explosion (Lunnan et al. 2018), making it a prime candidate for a PPISN. Upcoming transient surveys such as the ZTF (Bellm 2014; Smith et al. 2014) and the LSST (Abell et al. 2009) will detect similar events in large numbers, providing vital information to establish or discard their origin as pairinstability-driven transients (although note that the light echo of iPTF16eh was detected through flash spectroscopy and would be missed by photometric surveys).

In this context, the detection of merging binary BHs (BBHs) by the advanced LIGO (aLIGO) and Virgo (aVirgo) detectors (Abbott et al. 2016) can provide indirect evidence of the existence of PISNe and PPISNe. If these sources are formed via stellar binary evolution in the field, PISNe are expected to produce a clear gap in the observed masses of merging BBHs (Belczynski et al. 2014; Marchant et al. 2016). PPISNe are expected to widen this gap, as BH progenitors just below the PISN threshold can lose more than $10\,M_\odot$ before collapse (Woosley 2017). Given the sensitivity of the aLIGO detectors and the reported BBH mergers at the time, Fishbach & Holz (2017) showed that there was an indication of an upper mass cutoff of $\sim 40\,M_\odot$, consistent with models of field binary evolution that include both PISNe and PPISNe (Belczynski et al. 2016a;

Spera & Mapelli 2017). The recent release of the first Gravitational Wave Transient Catalog by the LIGO-Virgo Collaboration includes a total of 10 BBH merger detections (Abbott et al. 2018a) and strongly favors a dearth of BH masses above $45\,M_\odot$ (Abbott et al. 2018b).

Theoretical work to explain the formation of merging compact objects was driven at first by the discovery of the Hulse-Taylor binary pulsar (Hulse & Taylor 1975). Commonenvelope (CE) evolution, which had been proposed by Paczynski (1976) as the formation mechanism of cataclysmic variables, was invoked by van den Heuvel (1976) to reduce the orbital separations of wide massive binaries and produce close binary neutron stars. As it was realized that the Hulse-Taylor pulsar would coalesce owing to gravitational wave (GW) emission, population synthesis studies were done to understand the rate of such events in the context of CE evolution (Clark et al. 1979). More than a decade later, CE evolution was also proposed to form merging BBHs (Tutukov & Yungelson 1993), and it was proposed that BBH mergers would be the dominant sources detectable by ground-based GW observatories (Lipunov et al. 1997; see Dominik et al. 2012; Belczynski et al. 2016b, for more recent work).

Various additional channels have been put forward to explain the origin of merging BBHs. In very close binaries, efficient rotational mixing has been predicted to lead to merging BBHs, as chemically homogeneous evolution (CHE) prevents the expansion of a star during its main sequence (Maeder 1987) and allows for an initially compact binary to remain so until BH formation (Mandel & de Mink 2016; Marchant et al. 2016; de Mink & Mandel 2016). BBHs can also be formed through dynamical interactions in dense environments (Kulkarni et al. 1993; Sigurdsson & Hernquist 1993), with large systems such as globular clusters producing BBHs compact enough to merge (Portegies Zwart & McMillan 2000). Other scenarios include formation in triple-star systems (see Thompson 2011; Antonini et al. 2014, 2017) and active galactic nucleus disks (Bartos et al. 2017; Stone et al. 2017).

The objective of this work is to study the implications of PPISNe occurring with nearby binary companions and what effects the pulses have on the resulting BHs that could be observed through the detection of GWs in BBH mergers. To do this, we perform detailed simulations of the formation of BHs from single helium stars undergoing PPISNe. These are appropriate to model BBHs formed through binary evolution, including the CE and CHE channels, where each star is expected to become hydrogen-poor at its surface before BH formation. In Section 2 we describe our methods and present our PPISN models in Section 3. In Section 4 we discuss how the presence of a nearby companion can affect the occurrence of a PPISN, and in Section 5 we describe how PPISNe affect the observable properties of a merging BBH. We conclude with a discussion of our results in Section 6. All our models are available for download at 10.5281/zenodo.1211427, including the input files to perform these simulations, machine readable tables, and movies for each of our simulations.

2. Methods

We compute a set of nonrotating models of helium stars at a metallicity of $Z_{\odot}/10$, defining $Z_{\odot}=0.0142$ as the proto-solar abundance reported by Asplund et al. (2009). Our simulations are computed using version 11123 of the MESA software

instrument for stellar evolution (Paxton et al. 2011, 2013, 2015, 2018). Radiative opacities are computed using tables from the OPAL project (Iglesias & Rogers 1996). Convective regions are determined using the Ledoux criterion and convective energy transport, and mixing is modeled using a prescription for time-dependent convection that we describe in Appendix A. Regions that are stable according to the Ledoux criterion but unstable according to the Schwarzschild criterion undergo semiconvective mixing, which we model following Langer et al. (1983) with an efficiency parameter of $\alpha_{sc} = 1$. Overshooting from convective boundaries is modeled using exponential overshooting (Herwig 2000) with a parameter f = 0.01. Note that, formally, convective velocities are zero at the edge of a convective zone, such that an additional parameter f_0 is required to define exponential overshooting. The evaluation of the exponentially decaying mixing coefficient is then done at a distance f_0H_P inside the convective boundary, and we choose a value of $f_0 = 0.005$. Our chosen treatment softens convective boundaries and allows convective regions to expand against steep composition gradients. As a reference, Herwig (2000) finds that f = 0.016 is required for convective hydrogen-burning cores to reproduce the width of the main sequence.

Nuclear reactions are computed using the basic, co_burn, and approx21 nuclear networks provided in MESA, which are switched during runtime to account for different phases of nuclear burning. In particular, during pulsational phases we use the approx21 network. We provide a detailed description of this 21-isotope network and discuss how appropriate it is for these evolutionary phases in Appendix B, where we also present the results of a convergence test using a larger network. Nuclear reaction rates are taken from Caughlan & Fowler (1988) and Angulo et al. (1999), with preference given to the latter when available.

Our modeling of stellar winds follows that of Brott et al. (2011). All our models are hydrogen depleted at their surface, so we adopt the mass-loss rates of Hamann et al. (1995), scaled by a factor of 1/10 to account for the effect of clumping (Yoon et al. 2010). Although we only model naked helium stars, as we will show in Section 4, energy deposited by a PPISN on the outer layers can make the envelope of these stars expand, requiring also a recipe for winds from cool stars. For this purpose we take the mass-loss rate to be the maximum between the mass-loss rates of Nieuwenhuijzen & de Jager (1990) and 1/10 of the rate from Hamann et al. (1995). The rates provided by Nieuwenhuijzen & de Jager (1990) are calibrated using stars on our galaxy, so to account for lower mass-loss rates at lower metallicities, we scale it by a factor of $(Z/Z_{\odot})^{0.85}$. This assumes that the scaling of cool winds with metallicity follows the dependence for hot stars derived by Vink et al. (2001), which is consistent with observations of OB stars in the Galaxy and the Magellanic Clouds (Mokiem et al. 2007).

2.1. Modeling of PPISNe

Up to central helium depletion we assume hydrostatic equilibrium in our models. At later phases, we consider the weighted value of the first adiabatic exponent,

$$\langle \Gamma_{\rm l} \rangle = \frac{\int_0^M \frac{\Gamma_{\rm l} P}{\rho} dm}{\int_0^M \frac{P}{\rho} dm}, \qquad \Gamma_{\rm l} = \left(\frac{\partial \ln P}{\partial \ln \rho}\right)_{\rm ad},$$
 (1)

where M is the total mass of the star. The condition $\langle \Gamma_1 \rangle < 4/3$ can then be used as an approximate stability criterion (see Stothers 1999) to determine when the assumption of hydrostatic equilibrium is inappropriate. In our simulations, whenever $\langle \Gamma_1 \rangle - 4/3 <$ 0.01 and the central temperature exceeds 109 K, instead of assuming hydrostatic equilibrium we use the HLLC solver for hydrodynamics (Toro et al. 1994), which has recently been implemented into MESA (Paxton et al. 2018). This method can accurately model shocks and preserve energy, without requiring the use of an artificial viscosity. To account for iron core collapse or rapid evolution due to neutrino emission before the onset of dynamical instability, we also switch to the HLLC solver if the central temperature exceeds 10^{9.6} K or the neutrino luminosity is above $10^{10} L_{\odot}$. Wind mass loss is ignored when the HLLC solver is in use. For models that result in PPISNe and PISNe, we define the first instance when $\langle \Gamma_1 \rangle - 4/3 < 0.005$ as the pre-SN stage.

Modeling PPISNe is particularly challenging, as after a pulse the star can settle back into hydrostatic equilibrium and undergo periods of quiescence of more than 1000 yr (Woosley 2017). As the ejected layers expand and cool down, they become optically thin and go outside the range of applicability of MESA. To avoid this, during these long interpulse periods we remove the unbound layers as described in Appendix C and switch to a hydrostatic model if the conditions to turn on hydrodynamics described above are not met.

In order to distinguish individual pulses from our models, we compute at each step the maximum velocity in the inner 95% of the star that remains below the local escape velocity $v_{\rm esc} =$ $\sqrt{2Gm/r}$, which we define as v_{95} . Whenever $|v_{95}| > 20$ km s⁻¹, we consider that instant to be the beginning of a pulsation. After this point, we consider a pulse to finish once the inner layers are close to hydrostatic equilibrium. To do this, we take into account a dynamical timescale $\tau_{95} = 1/\sqrt{G \langle \rho \rangle_{95}}$, where $\langle \rho \rangle_{95}$ is the average density of the inner 95% of mass that remains bound. Whenever $|v_{95}| < 20 \text{ km s}^{-1}$ for a time longer than $20\tau_{95}$, or if the star undergoes iron core collapse, we consider the pulse finished. Even if the conditions for our definition of a pulse are met, we discard it if it results in ejections of less than $10^{-6} M_{\odot}$, which also prevents iron core collapse from being defined as a pulse. Although the values chosen are arbitrary, we have verified for all models computed that they match a by-eye definition of each mass ejection. Having a well-defined criterion gives us a way to unambiguously identify each pulsation.

Except for cases that are near the limit between PPISNe and PISNe, all our models that undergo iron core collapse have final masses in excess of $20\,M_\odot$. For such large core masses we expect a BH to be formed through direct collapse (Fryer 1999), and for all our models we assume that the final BH mass $M_{\rm BH}$ is equal to the baryonic mass before iron core collapse. Note, however, that some recent simulations have resulted in BH formation through fallback in a successful explosion, instead of direct collapse, even for such massive helium cores (Chan et al. 2018; Kuroda et al. 2018; Ott et al. 2018). This would further reduce the mass of the final remnant.

3. Single-star Models

Before discussing the overall properties of our models, we show the evolution of two representative PPISN simulations corresponding to helium stars with initial masses of 46 and

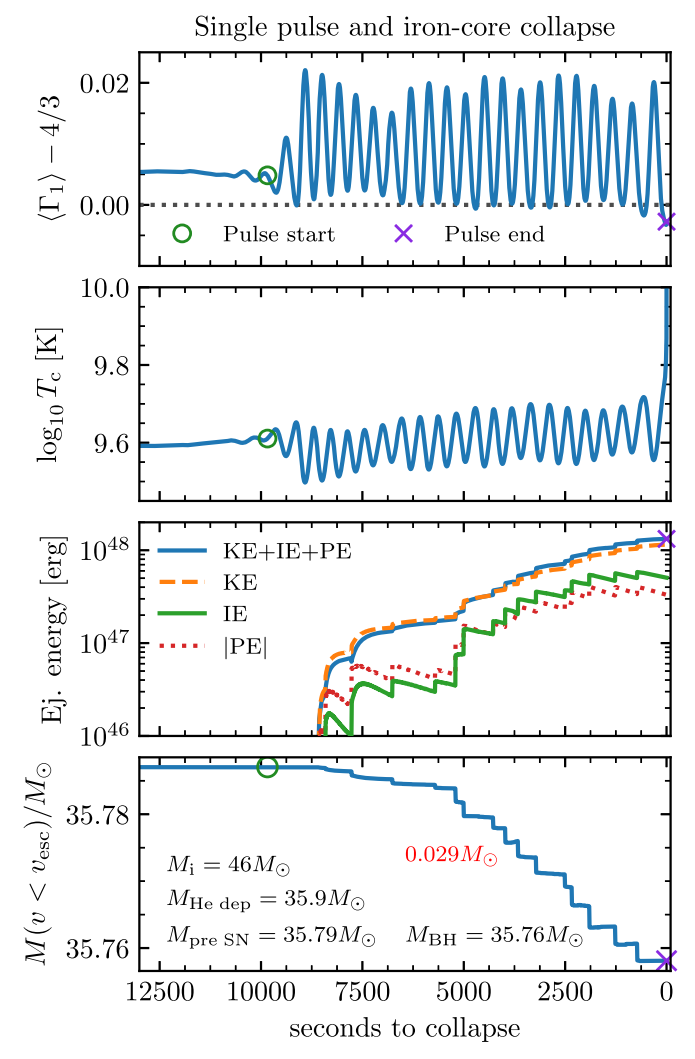


Figure 1. Evolution of a PPISN from a helium star model with an initial mass $M_i = 46~M_{\odot}$. Panels show the evolution with time of the average $\langle \Gamma_l \rangle$ (see Equation (1)), the central temperature, the energy of layers ejected due to the pulse, and the total mass of the star that remains below the escape velocity. The energy of ejected layers is also separated into its kinetic energy (KE), internal energy (IE), and potential energy (PE). The mass ejected through the pulse is written down in red in the bottom panel. Symbols are also used to denote the beginning and the end of the pulse as defined in Section 2.1.

 $76\,M_\odot$ and compare their mass loss and kinetic energy of ejecta to the models of Woosley (2017), which are computed at zero metallicity and without winds.

The $46~M_\odot$ model reaches core helium depletion with a mass of $M_{\rm He~dep}=35.9~M_\odot$. It then undergoes hydrostatic core carbon burning and hydrostatic core oxygen burning. Only after oxygen in the core has been depleted does the star contract into the pair-creation region, leading to a reduced $\langle \Gamma_l \rangle$. As the star approaches $\langle \Gamma_l \rangle = 4/3$, it starts experiencing oscillations, and the burning of carbon and oxygen in shells provides sufficient energy to eject $0.0289~M_\odot$ with a kinetic energy of 1.2×10^{48} erg, as shown in Figure 1. Only 3 hr pass from the onset of the instability to iron core collapse, and the star never recovers hydrostatic equilibrium during this time. According to our definition in the previous section, we then consider this to be an individual pulse, ⁵ after which a $35.8~M_\odot$ BH is formed.

Note that this definition is different from the PPISN calculations of Woosley (2017), who labels each individual oscillation in such cases as a "weak pulse."

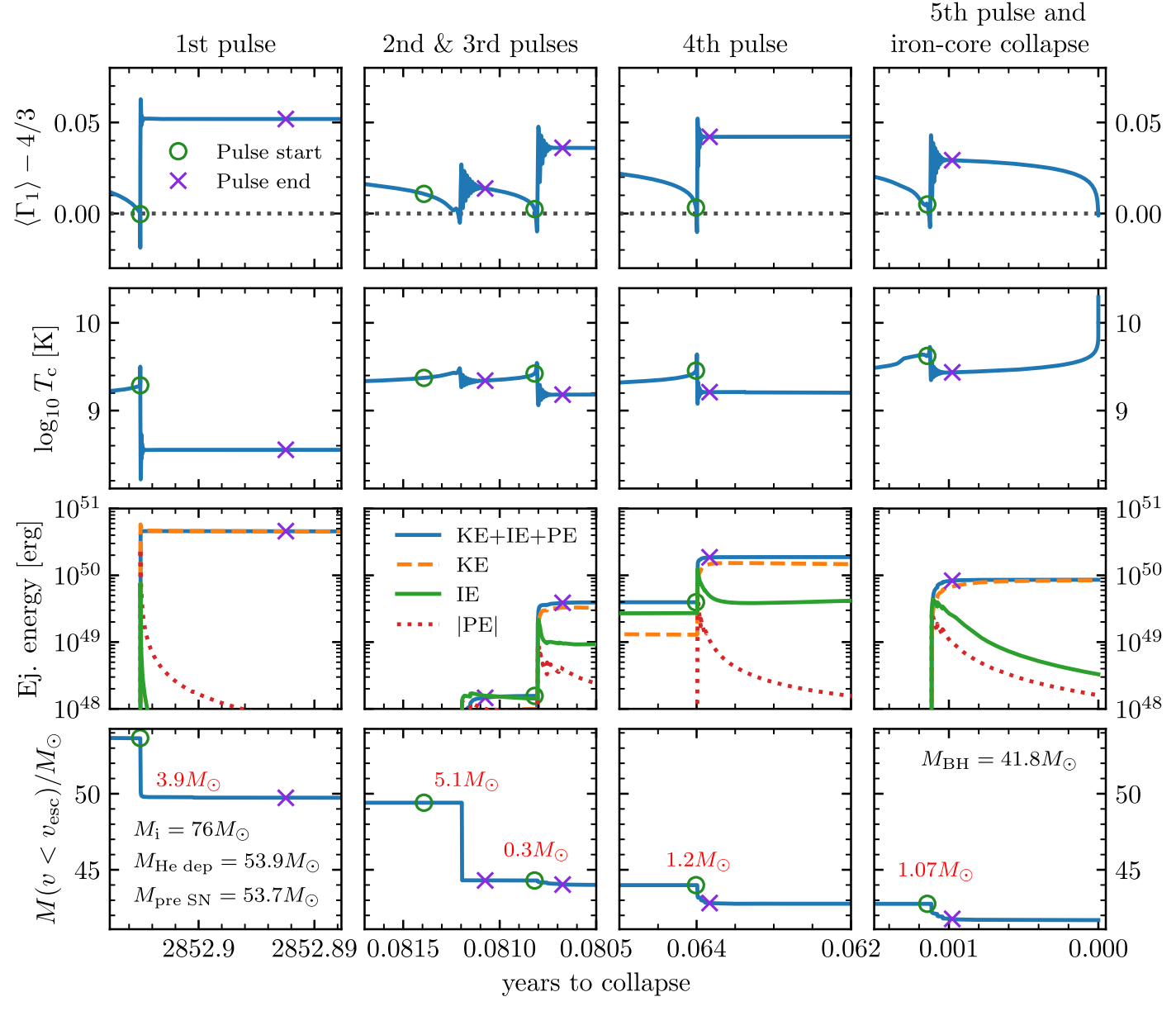


Figure 2. Same as Figure 1, but for a PPISN model with an initial mass $M_i = 76 M_{\odot}$. This star, however, undergoes a single phase of dynamical instability before iron core collapse. Each set of vertical panels shows a zoomed-in time evolution during different pulses.

The 76 M_{\odot} model also results in a PPISN, but its evolution is dramatically different. This simulation reaches core helium depletion with its mass lowered to $M_{\rm He\ dep} = 53.9\ M_{\odot}$ owing to stellar winds, after which it undergoes hydrostatic core carbon burning. Pair creation then leads to a reduced $\langle \Gamma_1 \rangle$ and dynamical instability before core oxygen ignition, and we depict its pulsational stage in Figure 2. When $\langle \Gamma_1 \rangle - 4/3 <$ 0.005, which is the point we have defined as the pre-SN stage, winds have further reduced the mass of the star by $0.2 M_{\odot}$ down to $M_{\rm pre~SN}=53.7~M_{\odot}$. At this moment it experiences a strong pulsation that removes $3.94 M_{\odot}$ with a kinetic energy of 5×10^{50} erg and lowers the central temperature by almost a factor of 4 compared to its value at the beginning of the pulse. The star then has a long quiescence phase lasting almost 3000 yr, until it again becomes pulsationally unstable, leading to additional pulses and mass loss within a month of iron core collapse. Although a pulse happens just 3 days prior to iron core collapse,

the star returns to equilibrium and undergoes hydrostatic core silicon burning before collapsing to a $41.8\,M_\odot$ BH.

This large difference on the timescale from the onset of pulsations to iron core collapse is due to the neutrino luminosity decreasing steeply with central temperature (Woosley et al. 2007; Yoshida et al. 2016; Woosley 2017). As more massive models experience more energetic pulses, their post-pulse central temperatures are lower, resulting in photon radiation from the surface becoming the main energy-loss mechanism instead of neutrino emission. For example, in the first pulse of our $76\,M_\odot$ model the neutrino luminosity at the pre-SN stage is in excess of $10^{12}\,L_\odot$, and at the end of the pulse it has lowered to $\sim 1.5 \times 10^4\,L_\odot$. The main source of energy loss at this point is just radiation from its surface, so the star evolves on the ~ 1000 yr long Kelvin–Helmholtz timescale. Matching the pre-SN mass of our models to the initial masses of the models of Woosley (2017), we find a good qualitative agreement. His $36\,M_\odot$ model

Table 1 Hydrogen-free PPISN Models at Low Metallicity ($Z=Z_{\odot}/10$)

$M_{ m initial} \ (M_{\odot})$	$M_{ m He\ dep} \ (M_{\odot})$	$M_{ m CO} \ (M_{\odot})$	$M_{ m pre~SN} \ (M_{\odot})$	$M_{ m He,\ pre\ SN} \ (M_{\odot})$	$M_{ m ejecta} \ (M_{\odot})$	$M_{ m BH} \ (M_{\odot})$	No. of Pulses	Duration (yr)	Max KE 10 ⁵¹ (erg)
40.00	31.99	27.69	•••	•••		31.87	0	•••	
42.00	33.32	28.92				33.19	0		
44.00	34.63	30.12				34.50	0		
44.50	34.95	30.42				34.82	0		
45.00	35.28	30.72	35.14	0.69	0.02	35.13	1	0.000139	0.000785
45.50	35.60	31.02	35.46	0.67	0.01	35.45	1	1.89×10^{-5}	0.000561
46.00	35.92	31.32	35.79	0.68	0.03	35.76	1	0.00029	0.00115
48.00	37.21	32.50	37.06	0.67	0.04	37.02	1	0.00129	0.00127
50.00	38.47	33.67	38.32	0.65	0.24	38.08	3	0.00273	0.0113
52.00	39.73	34.82	39.57	0.64	0.66	38.90	4	0.00677	0.0292
54.00	40.97	35.96	40.80	0.63	0.25	40.55	5	0.00485	0.00929
56.00	42.20	37.08	42.02	0.63	0.33	41.69	7	0.00773	0.0145
58.00	43.41	38.21	43.23	0.62	1.62	41.60	9	0.0303	0.108
60.00	44.62	39.32	44.42	0.61	1.72	42.70	9	0.0388	0.128
62.00	45.81	40.42	45.61	0.60	2.51	43.10	10	0.135	0.0549
64.00	47.00	41.50	46.79	0.60	4.12	42.67	6	0.622	0.171
66.00	48.17	42.57	47.95	0.59	4.55	43.41	9	1.37	0.19
68.00	49.33	43.66	49.11	0.58	5.29	43.82	10	11	0.202
70.00	50.49	44.70	50.26	0.58	6.31	43.94	11	132	0.163
72.00	51.64	45.75	51.40	0.57	8.02	43.31	6	732	0.254
74.00	52.78	46.80	52.53	0.57	9.61	42.72	4	1.9×10^{3}	0.409
76.00	53.92	47.87	53.66	0.56	11.66	41.69	5	2.85×10^{3}	0.578
78.00	55.05	48.89	54.79	0.56	14.06	40.33	5	3.84×10^{3}	0.814
80.00	56.18	49.94	55.91	0.55	16.81	38.64	5	4.67×10^{3}	1.14
82.00	57.31	50.97	57.02	0.55	19.22	37.33	5	5.38×10^{3}	1.47
84.00	58.42	52.00	58.13	0.54	23.73	33.94	6	6.18×10^{3}	1.94
86.00	59.51	53.01	59.20	0.54	28.98	29.89	9	7.13×10^{3}	2.57
87.00	60.04	53.49	59.73	0.54	31.66	27.82	2	7.5×10^{3}	2.78
88.00	60.58	54.01	60.27	0.54	41.58	18.60	2	9.72×10^{3}	3.18
88.50	60.85	54.27	60.54	0.54	45.26	15.22	1	1.08×10^{4}	3.3
88.75	60.96	54.38	60.65	0.54	46.97	13.63	1	1.14×10^{4}	3.34
89.00	61.10	54.48	60.79	0.54	49.18	11.57	1	1.29×10^4	3.43
89.05	61.13	54.52	60.81	0.54	60.81		1		3.5358
90.00	61.64	54.95	61.32	0.53	61.32		1	•••	3.7902
100.00	66.80	59.77	66.44	0.52	66.44		1		7.8267
150.00	89.93	81.23	89.37	0.50	89.37		1	•••	32.069
200.00	109.61	99.63	108.84	0.50	108.84		1		57.553
240.00	123.37	112.59	122.43	0.50	122.43		1	•••	63.129
242.00	124.12	113.29				123.18	0	•••	
250.00	126.61	115.65	•••	•••		125.64	0	•••	
290.00	138.87	127.14	•••	•••		137.74	0	•••	

Note. Initial and final properties of helium stars with a metallicity of $Z_{\odot}/10$ undergoing PPISNe. We define helium depletion as the point in time where the central helium mass fraction drops below 0.01. CO core masses are defined when the central helium mass fraction drops below 10^{-3} as the innermost mass coordinate where the helium mass abundance is larger than 0.01. For pulsating models $M_{\rm pre~SN}$ is the mass at the onset of pulsations, defined as the moment when $\langle \Gamma_l \rangle - 4/3 < 0.005$, and $M_{\rm He,~pre~SN}$ is the total mass of helium at this point. Note that the difference between $M_{\rm pre~SN}$ and $M_{\rm BH}$ is not exactly equal to $M_{\rm ejecta}$, despite our assumption of the BH mass being equal to the baryonic mass before iron core collapse. This difference is due to wind mass loss during phases of quiescence after the onset of the first pulse.

results in the ejection of $0.18\,M_\odot$, with a kinetic energy of 3.7×10^{48} erg, and takes $18,000\,\mathrm{s}$ from the onset of instability until iron core collapse. The $54\,M_\odot$ model of Woosley (2017) ejects $6.58\,M_\odot$ in four pulses, with a total kinetic energy of 9.4×10^{50} erg, and takes 150 yr from the onset of pulsations to iron core collapse. Except for the time to collapse of the more massive model, all these numbers match within a factor of a few to our results, which is remarkable given how steeply they change with the mass of the progenitor and the different initial conditions used. For example, the $56\,M_\odot$ simulation of Woosley (2017) takes $\sim 1000\,\mathrm{yr}$ to undergo iron core collapse from the beginning of the pulsational phase.

3.1. Grid of Models

We compute models of nonrotating pure helium stars in the range of initial masses $M_{\rm initial}=40\text{--}100\,M_{\odot}$ at intervals of $2\,M_{\odot}$, with a finer mass resolution near the edges to better resolve the minimum mass for a PPISN to occur and the boundary between PPISNe and PISNe. For completeness, we also include models with initial masses $>100\,M_{\odot}$ to resolve the upper mass limit at which BHs are formed again. These are summarized in Table 1. The lower-mass model of $40\,M_{\odot}$ undergoes regular iron core collapse and no eruptions, while the $89.05\,M_{\odot}$ model is completely disrupted in a PISN. PPISN models with initial masses between 45 and $48\,M_{\odot}$ experience small-amplitude pulsations and never restore their hydrostatic

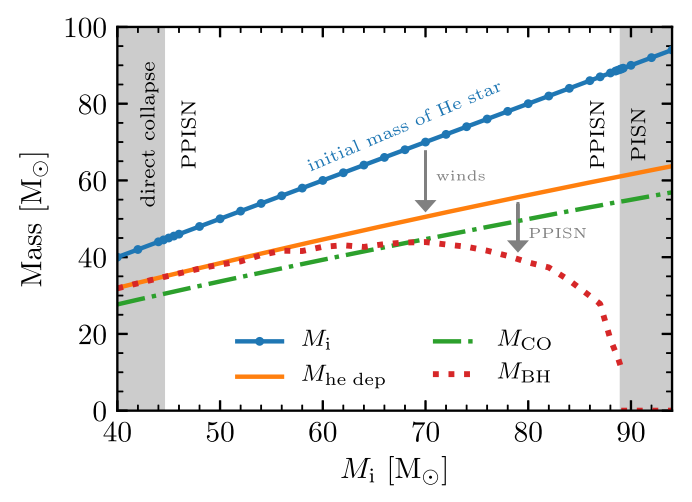


Figure 3. Masses at different evolutionary stages for PPISN models as a function of the initial mass M_i . $M_{\text{He dep}}$ and M_{CO} are the total and CO core masses at helium depletion, while M_{BH} is the final mass of the BH formed. Individual circles in the blue M_i line indicate individual simulations that were performed.

equilibrium, as exemplified by the $46\,M_\odot$ model shown in Figure 1. All other PPISN models manage to restore hydrostatic equilibrium after the first pulsation and have phases of quiescence before iron core collapse. All PPISN and PISN models undergo the first pulse with $\sim\!0.5\,M_\odot$ of helium left. Despite strong mass loss, during core helium burning the convective core recedes as mass is lost, and the time between core helium depletion and the onset of the SN is never enough to fully remove the remaining helium in the outer layers.

For models at zero metallicity and without mass loss, Woosley (2017) finds a range for occurrence of PPISNe between 34 and $62\,M_{\odot}$. This can be compared to the range of pre-SN masses, $M_{\rm pre~SN}=35.1$ – $60.8\,M_{\odot}$, at which we find PPISNe. Despite our models being at a finite metallicity of $Z_{\odot}/10$ and including mass loss, we see that both the lower and upper mass limits for the occurrence of PPISNe we obtain are consistent with those of Woosley (2017).

We show the resulting BH masses for our PPISN simulations in Figure 3. Models up to $M_{\rm i}=56\,M_{\odot}$ ($M_{\rm pre~SN}\simeq42\,M_{\odot}$) undergo pulsations for less than a week and remove less than 1% of the mass of the star prior to iron core collapse, resulting in only a small change in the final BH mass. Models above $M_{\rm i}=70\,M_{\odot}$ ($M_{\rm pre~SN}\simeq50\,M_{\odot}$) lose more than 10% of their mass through pulsations and take from hundreds to 10,000 yr between their first pulse and iron core collapse. These stars eject a significant fraction of their CO cores, resulting in a monotonically decreasing $M_{\rm BH}$ as a function of $M_{\rm i}$.

We find the boundary between PPISNe and PISNe to be between our models with pre-SN masses of $M_{\rm pre~SN}=60.79~M$ and $60.81~M_{\odot}~(M_{\rm i}=89~{\rm and}~89.05~M_{\odot})$, with the $M_{\rm pre~SN}=60.79~M_{\odot}$ star resulting in a $\sim 12~M_{\odot}~{\rm BH}$. We find that the final BH mass cannot be made arbitrarily small by considering models closer to the PISN limit; the inner $\sim 10~M_{\odot}$ of the $M_{\rm pre;SN}=60.81~M_{\odot}$ simulation actually reaches hydrostatic equilibrium after the pulse, but it is finally disrupted on a longer timescale by the decay of radioactive nickel produced during the pulse. What is important to emphasize here is that there is a physical process that sets a nonzero value for the minimum remnant mass a PPISN can produce. The particular values of $M_{\rm pre~SN}=60.79~M$ and $60.81~M_{\odot}$ simply illustrate the sharp

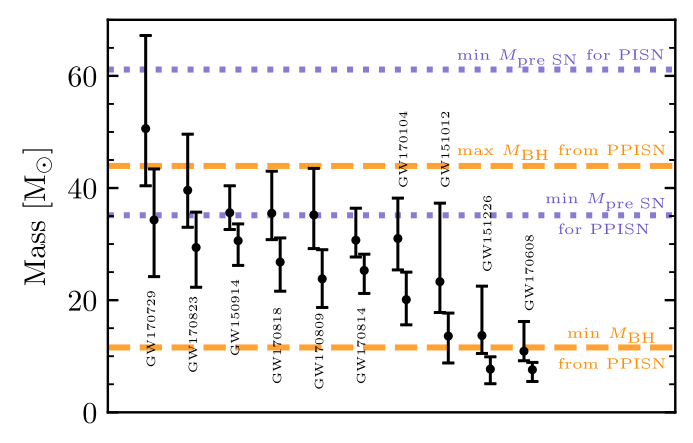


Figure 4. Masses of individual BHs in observed BBH mergers from the first Gravitational Wave Transient Catalog, ordered by total mass. Dotted horizontal lines indicate the range in $M_{\text{pre SN}}$ for the occurrence of a PPISN in our models, with stars just above this range resulting in total disruption in a PISN. Dashed lines indicate the range of BH masses produced by PPISN.

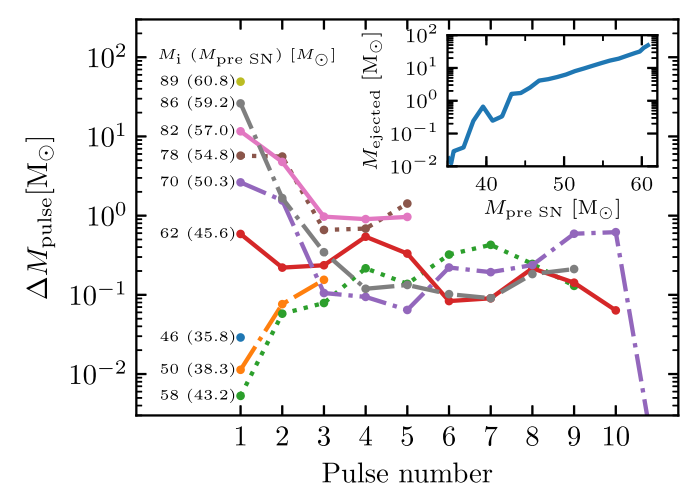


Figure 5. Mass lost in individual pulses for a few representative models.

transition between PPISNe and PISNe but should not be interpreted as resolving the threshold to within $0.02\,M_\odot$. As we show in Appendix B, our choice of a 21-isotope nuclear reaction network can produce $\sim\!10\%$ errors in nickel yields when compared to more detailed networks, and the exact value for the transition between PPISNe and PISNe will be modified by this.

Figure 4 shows the masses of individual BHs for all BBH mergers observed so far, as reported in the first Gravitational Wave Transient Catalog (Abbott et al. 2018a). In particular, within the 90% confidence intervals the more massive BH in GW170729 has a mass that exceeds the minimum $M_{\text{pre SN}}$ required for a PPISN and even reaches beyond the minimum $M_{\text{pre SN}}$ required for a PISN. Within the large uncertainties reported in individual masses, all primary BHs except those of GW151226 and GW170608 have masses larger than the minimum $M_{\text{pre SN}}$ required for a PPISN, making them consistent with being the product of a weak PPISN event. Since for higher-mass PPISN progenitors the final BH mass can be as low as $\sim 12 M_{\odot}$, all of the BHs measured in BBH mergers (except for the secondaries in GW151226 and GW170608) could be the product of the evolution of $M_{\rm initial} > 70\,M_{\odot}$ helium cores with high PPISN mass loss. However, we expect

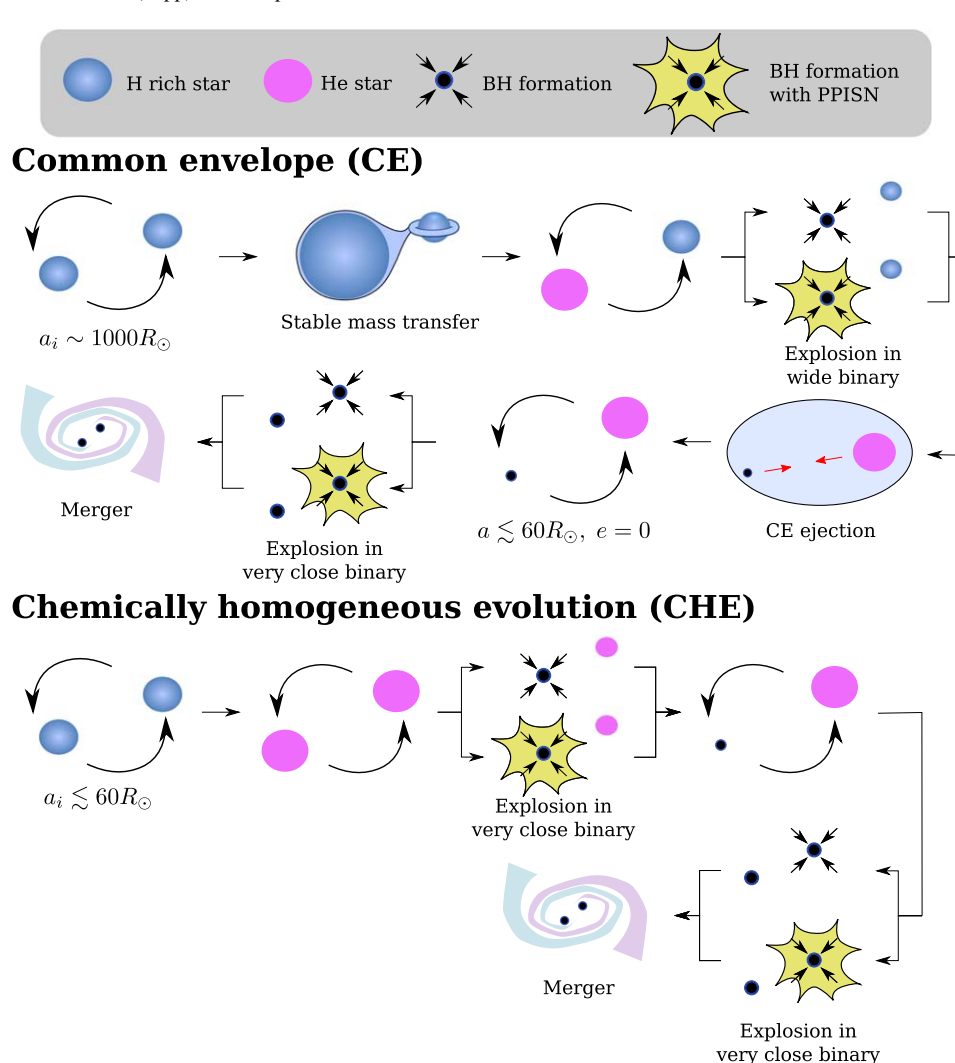


Figure 6. Possible occurrence of PPISNe in two different formation channels for merging BBHs through field binary evolution. The limit $a \lesssim 60$ is required for a $40 M_{\odot} + 40 M_{\odot}$ BBH to merge in less than 13.8 Gyr, while separations $a > 1000 R_{\odot}$ are typical in the formation scenario of BHs similar to GW150914 through CE evolution (see Belczynski et al. 2016b).

this to be unlikely, as the initial mass function disfavors such massive progenitors and they are more likely to be the result of collapse from lower-mass progenitors. We obtain an upper limit of $\sim\!44\,M_\odot$ for the mass of BHs formed through PPISNe, which is in good agreement with the results from the LIGO-Virgo Collaboration that find that the observed sample is well described by models that have $<\!1\%$ of BHs with masses above $45\,M_\odot$ (Abbott et al. 2018b).

We dissect the individual mass loss from each pulse in Figure 5. Lower-mass stars experience progressively larger pulses, while the opposite is the case for the more massive systems. In addition to this, the more massive models experience a long period of quiescence (up to tens of thousands of years) between the first and the second pulse (see Table 1). It is these long-lived objects that we focus on in the following section.

4. Impact of Close Companions in a PPISN

If merging BBHs can be formed by binaries in the field, we expect PPISNe from hydrogen-depleted stars to occur at different stages in their evolution if they involve massive enough stars. This is illustrated in Figure 6 for two different

cases: (i) CE evolution in wide binaries and (ii) CHE in very close binaries. In both cases a BBH can be formed where either one or both components underwent a PPISN. For the CE channel, a PPISN can happen with a companion in a wide orbit ($a \sim 1000\,R_\odot$) if it collapses before the envelope is ejected through a CE, or in a compact orbit ($a \lesssim 60\,R_\odot$) if it happens after envelope ejection. In the case of CHE, two PPISNe from hydrogen-free progenitors in a compact orbit are possible.

So far we have considered PPISNe to be unaffected by a nearby binary companion. However, during a pulse heat is deposited throughout the entire star, causing the post-pulse remaining layers to have a much more extended radius than the starting object. We focus here on the systems that have long lifetimes after their first pulse, studying the evolution of models with $M_i \ge 70 \, M_\odot$ ($M_{\rm pre~SN} \ge 50.3$), which are quiescent for more than a century between the first and second mass ejection.

4.1. Interaction Right after a Pulse

We first consider interaction happening immediately after a pulse in a very close binary, close enough for the resulting system to merge from the emission of GWs in less than the age of the universe, 13.8 Gyr (Ade et al. 2016). For this purpose,

we take as a characteristic companion a $40\,M_\odot$ star or BH (characteristic of the BH masses resulting from PPISNe; see Table 1) at a separation of $a=58.6\,R_\odot$. This corresponds to the minimal separation required for a $40\,M_\odot+40\,M_\odot$ BBH to merge in less than $t_m=13.8\,\mathrm{Gyr}$ (Peters 1964). Even accounting for enhanced eccentricity due to the mass ejection, the final distance at periastron has to be $\leqslant 58.6\,R_\odot$ for a merger to happen within 13.8 Gyr, so it can be used as an upper limit to determine whether a binary close enough to merge from GW emission would interact after the pulse.

The radial evolution through the first pulse of three of our simulations is shown in Figure 7. An $M_i=70\,M_\odot$ progenitor has a radius below $1\,R_\odot$ before the first pulse. After the pulse, the outer layers expand significantly, in particular the radius at a mass coordinate corresponding to 99% of the mass that remains bound expands by two orders of magnitude. At the end of the phase shown in Figure 7 there are $0.12\,M_\odot$ that extend beyond $r=58.6\,R_\odot$, such that the remaining star would start interacting with a binary companion close enough to result in a BBH merger. The 78 and $86\,M_\odot$ models present even more extreme behavior, with the pulse resulting in 0.41 and $1.3\,M_\odot$ remaining beyond our nominal choice of $a=58.6\,R_\odot$ at the end of the pulse. If these systems are to result in a merging BBH, then they should exhibit strong interaction, possibly evolving into a CE immediately after the pulsation.

Even if a significant amount of bound mass extends to regions beyond the orbital separation, it is not obvious that the resulting system will undergo an inspiral inside a CE. In particular, the time available before iron core collapse could be larger than the timescale for an inspiral due to frictional drag. To see if this is the case, we consider the models at the end points of Figure 7 and follow Taam et al. (1978) to estimate the energy dissipation rate due to the drag as

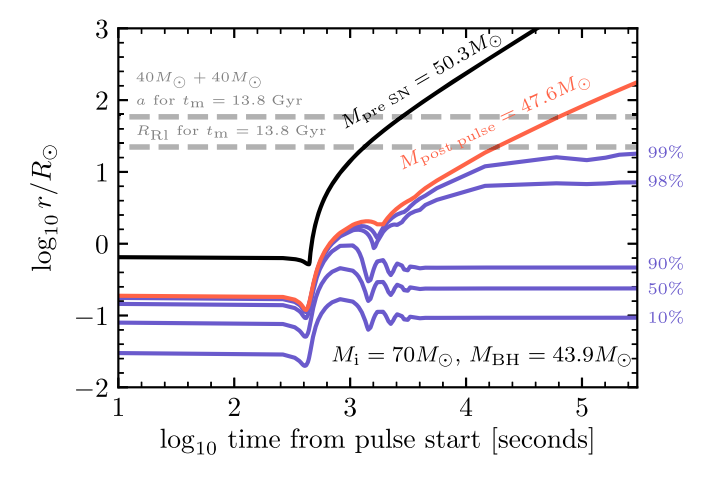
$$L_{\rm drag} = \pi R_A^2 \rho v_{\rm rel}^3, \tag{2}$$

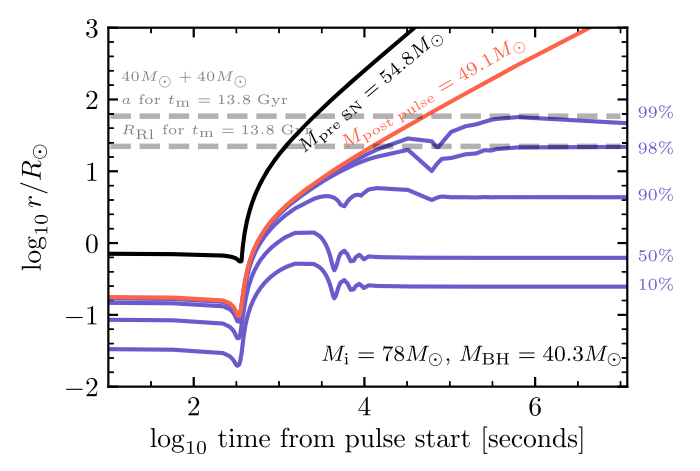
where R_A is the accretion radius, the density ρ is taken at the radial coordinate $r=58.6\,R_\odot$ of the post-pulse star, and $v_{\rm rel}$ is the relative velocity of the inspiraling companion and its surrounding envelope. For simplicity we consider a circular orbit with a separation $a=58.6\,R_\odot$ and component masses $M_1=M_{\rm post\;pulse}$ and $M_2=40\,M_\odot$. Assuming that the rotation velocity of the expanded layers is negligible since they rapidly expand by about two orders of magnitude, the relative velocity is simply the sum of the orbital velocities of both components and is of the order of $\sim 500\,{\rm km\,s^{-1}}$ for the three models we consider. The accretion radius can be computed as

$$R_A = \frac{GM_2}{v_{\rm rel}^2 + c^2},\tag{3}$$

where c is the local sound speed. We find R_A to be on the order of $\sim 20 R_{\odot}$. Since this is comparable to the orbital separation, in order to provide a conservative estimate of the drag, we use instead $R_A = H_P$, the local pressure scale height of the star at $r = 58.6 R_{\odot}$, which we find to be $\sim 10 R_{\odot}$ for these three models. The characteristic timescale for inspiral can then be estimated as

$$\tau_{\rm ins} = \frac{a}{|da/dt|}, \qquad \frac{da}{dt} = \frac{L_{\rm drag}}{GM_1M_2/2a^2}.$$
(4)





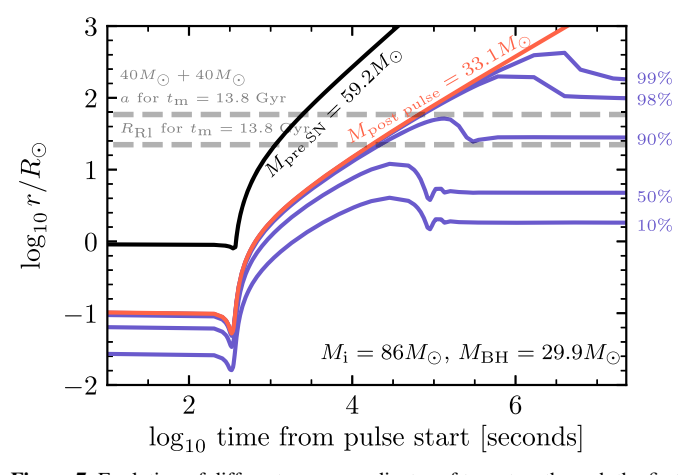


Figure 7. Evolution of different mass coordinates of two stars through the first PPISN pulse. Black lines indicate the pre-SN mass of the pulsating star, while orange lines indicate the remaining mass after the pulse (the mass coordinate where $v < v_{\rm esc}$). Purple lines indicate fixed mass fractions of the mass remaining after the pulse. For reference, the orbital separation (a) and Roche lobe radius ($R_{\rm Rl}$) for a 40 $M_{\odot}+40~M_{\odot}$ BBH to merge due to GW radiation in 13.8 Gyr are shown with horizontal dashed gray lines. At the end points shown for each of these simulations, 99% of the mass that remains bound is in hydrostatic equilibrium, and the outer layers are removed as described in Appendix C.

Computing this for our 70, 78, and $86 M_{\odot}$ progenitors results in $\tau_{\rm ins} = 28, 6.7$, and $1.6 \, \rm yr$, respectively. Since these stars are expected to live for more than a century before additional pulses

and iron core collapse occur, there is enough time for an inspiral to happen. Figure 8 shows how these results are modified by a different choice of orbital separation. In particular, for the 78 and $86\,M_\odot$ models, which have a lifetime >1000 yr after the first pulse, successful inspirals are expected even up to radii an order of magnitude larger than $a=58.6\,R_\odot$. Thus, the development of a CE inspiral is expected to happen for a wide range of separations.

Estimating the outcome of these inspirals is much more uncertain using our 1D models, considering that the star at this point has ejected almost all its helium and it is an extended CO core with no well-defined core envelope boundary. This adds to all the uncertainties associated with CE evolution (see Ivanova et al. 2013b). Despite the short inspiral timescales, the orbital separation and eccentricity will not necessarily be significantly affected by the CE. This is because a small reduction in the separation can provide enough energy to remove the relatively small amount of mass in the extended layers.

4.2. Interaction during Interpulse Phases

Even if the PPISN happens in a wide binary with $a > 1000 R_{\odot}$, we expect interaction to happen. Figure 9 shows tracks in the H-R diagram of the same $M_i = 70$, 78, and $86 M_{\odot}$ progenitors we discussed above, including the evolution before the first pulse and between the first pulse and the second. During the evolution after the first pulse, the ejected layers have been removed following the procedure described in Appendix C, so the luminosity and effective temperature shown correspond to the photosphere of the bound star that is left.

As convection develops in the outermost layers of these stars, they expand to become red supergiants with radii in excess of $1000 R_{\odot}$. These objects are quite peculiar, as through the pulsation all the helium-rich layers are ejected, resulting in a red supergiant composed almost entirely of carbon and oxygen at its surface. This expansion will result in Roche lobe overflow even for binaries at a separation $\sim 3000 R_{\odot}$. If this happens, mass transfer could be either stable or unstable depending on the mass ratio of the system and the response of the donor star to mass loss (Soberman et al. 1997). Unstable mass transfer would proceed on a dynamical timescale and could lead to a CE inspiral. If mass transfer is stable, we expect it to operate on the same timescale in which the star is expanding. This is the thermal timescale of this extended envelope, which is of the order of \sim 10,000 yr, such that subsequent PPISN pulses would happen while the star is still transferring mass to a companion. In the context of the CE formation channel of merging BBHs, the companion at this point would be a nondegenerate star most likely on the main sequence.

5. Impact of PPISNe on Merging BBHs

5.1. Change in Spin

Observationally, the spin of a merging BBH is constrained mostly in terms of the parameter $\chi_{\rm eff} = (m_1\chi_1 + m_2\chi_2)/(m_1 + m_2)$, where m_1 and m_2 are the individual masses of each BH and χ_1 and χ_2 their projected spin parameters on the orbital plane. There is an important degeneracy between $\chi_{\rm eff}$ and the mass ratio of the merging BBH, which limits the precision to which each can be measured independently (Hannam et al. 2013). Despite this, the measurements so far by the aLIGO and aVirgo detectors have shown that $\chi_{\rm eff}$ is centered around zero (Abbott et al. 2016), indicating that the BH spins are either small or significantly misaligned with the orbital plane.

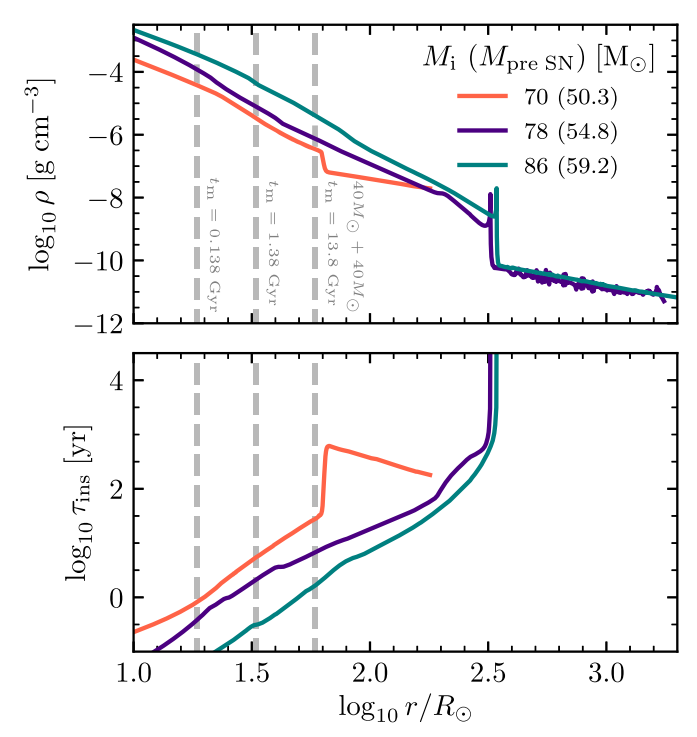


Figure 8. Top: density profiles of layers with velocities $v < v_{\rm esc}$ after the end of the first pulse for the three PPISN models shown in Figure 7. Dashed vertical lines indicate the separation required for a $40 \, M_{\odot} + 40 \, M_{\odot}$ BBH to merge owing to emission of GWs in 13.8, 1.38, and 0.138 Gyr. Bottom: inspiral timescale assuming a $40 \, M_{\odot}$ companion at a circular orbit with separation a = r (see Equation (4)).

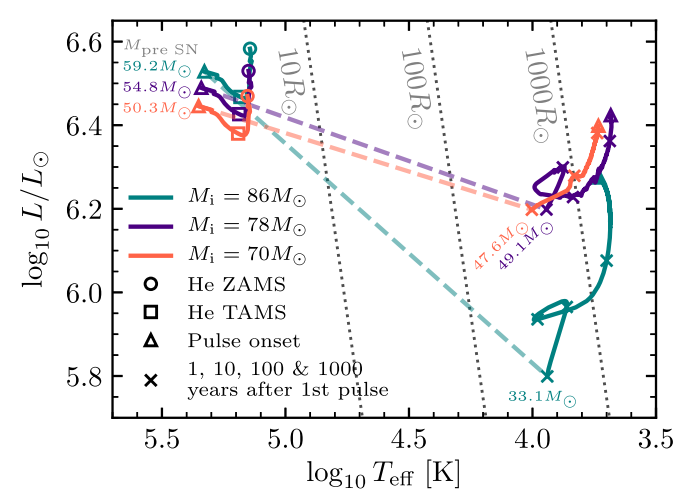


Figure 9. H-R diagram showing the evolution of helium star models with $M_i = 70$, 78, and $86 M_{\odot}$. Dashed lines connect the properties of the star at the onset of the first pulse and 1 yr afterward, with crosses indicating periods of time 1, 10, 100, and 1000 yr after the onset of the first pulse. Evolution after the onset of the second pulse is not shown but corresponds to less than 1 yr in time before iron core collapse. All models evolve to become CO red supergiants.

One potential source of orbit misalignment are kicks from asymmetric pulses and their associated mass loss. To our knowledge, there are no multidimensional simulations assessing how symmetric PPISN ejections are. Chen et al. (2014) performed 2D simulations of colliding shells from a PPISN but did not model their actual ejection, so it does not provide information on potential kicks produced on the remnant. For this discussion we ignore the effect of kicks on $\chi_{\rm eff}$ but note that they would only result in a reduction of it.

The spin parameter of a BH will depend on the distribution of angular momentum in its progenitor. Stellar winds are an efficient mechanism to remove angular momentum from a star (see Heger et al. 2005), as the long timescales involved allow for efficient coupling between the stellar envelope and its core. PPISN eruptions can remove a large fraction of the mass of a star, but in contrast to wind mass loss, they happen in a dynamical timescale of the star, preventing efficient coupling.

As we only consider nonrotating stellar models, we cannot self-consistently measure the impact of eruptions on the final BH spin. However, it can be approximated under a few assumptions. Consider the spin parameter at mass coordinate m, $a(m) = J(m)c/m^2G$, where J(m) is the angular momentum contained inside the mass coordinate m. If the star rotates as a solid body with an angular frequency ω , then $a(m) \propto \omega I(m)/m^2$, where I(m) is the moment of inertia of the star up to m. A rapid mass-loss event that reduces the mass of the star from $M_{\text{pre SN}}$ to M_f then produces a relative change in the spin of

$$\frac{a(M_f)}{a(M_{\text{pre SN}})} = \frac{I(M_f)}{I(M_{\text{pre-SN}})} \frac{M_{\text{pre SN}}^2}{M_f^2}.$$
 (5)

If the amount of mass loss during a PPISN does not depend strongly on rotation at the moment of collapse, we can use the final BH mass $M_{\rm BH}$ predicted by our models to compute the relative change in spin.

It has to be pointed out that there are clear caveats to this calculation, in particular, for the case of PISNe it is known that their evolution can be altered by rapid rotation, as progenitors can be stabilized owing to centrifugal forces and lead to weaker explosions (Glatzel et al. 1985; Chatzopoulos et al. 2013). Also, during late burning stages, the inner regions of a star are expected to decouple and rotate at higher angular frequencies than the outer layers (see Heger et al. 2000). These two effects are expected to reduce the angular momentum lost through eruptive mass loss, since they imply less mass loss and that the assumption of solid-body rotation overestimates the angular momentum of the outer layers. The estimate given by Equation (5) then represents the maximum effect PPISN mass loss can cause on the final BH spin.

Figure 10 shows the result of computing Equation (5) for some representative models in our grid spanning the entire PPISN range. Most systems only experience reductions of $\sim\!30\%$, and it can be seen that even for stronger pulses the spin cannot be reduced below 50% of its initial value. Although they produce a nonnegligible change in the spin, PPISN eruptions are not capable of reducing the effective spin of a progenitor with $\chi_{\rm eff}\sim 1$ down to the values observed by aLIGO/aVirgo. Kicks produced during PPISNe could further reduce $\chi_{\rm eff}$ by misaligning the orbit and the spin of the BH, but whether or not PPISNe could lead to strong kicks is uncertain.

5.2. Eccentricity Enhancement

It is expected that the upcoming LISA observatory will detect GWs from inspiraling BBHs up to years before they are detectable by ground-based observatories (Sesana 2016). This opens up the possibility of measuring eccentricities for these sources, which can be used to distinguish between formation scenarios (Nishizawa et al. 2016; Breivik et al. 2016). In particular, dynamical formation scenarios can produce highly eccentric BBHs (Rodriguez et al. 2016; Antonini et al. 2017), allowing them to be distinguished from BBHs produced

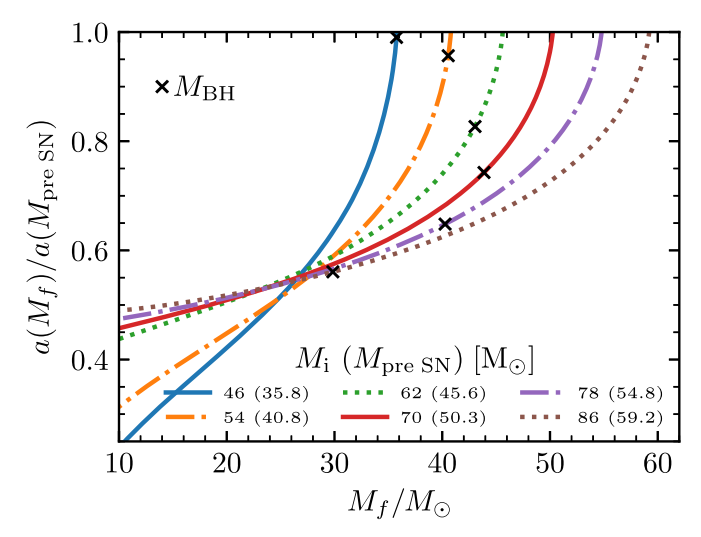


Figure 10. Final spin in terms of its initial one for eruptive mass loss. Each line indicates one of our models on the onset of collapse, and the black crosses indicate the final mass of the BH formed after undergoing a PPISN.

through field binary evolution. However, dynamical ejections of mass in field binaries can also change the eccentricity of these systems (Blaauw 1961; Boersma 1961).

In order to estimate whether mass loss through PPISNe can produce systems with measurable eccentricities in the LISA frequency band, we consider two different scenarios:

- The system is formed through CE evolution. In this case, the eccentricity induced by the first PPISN is erased by a CE phase. Only the second formed BH contributes to the final eccentricity when it undergoes a PPISN (see Figure 6).
- 2. The system is formed through CHE. In the absence of a CE phase, PPISNe from both stars contribute to the final eccentricity.

For both cases, in order to compute eccentricities at the moment of BBH formation, we assume the following:

- 1. Each mass ejection is completely symmetric and imparts no momentum kick on the layers that remain bound. We also ignore binary interaction in between pulsations and assume that the material is ejected at a velocity much larger than the orbital velocity. The resulting ejection is analogous to a Blaauw kick (Blaauw 1961) and therefore produces a change in orbital eccentricity that is independent of orbital separation.
- 2. A PPISN can undergo multiple pulses before collapsing, each affecting the orbital parameters in a different way depending on the orbital phase at the moment of the ejection. We assume that the orbital phase at each pulse has a flat distribution, as the periods of quiescence for PPISN models experiencing significant mass loss are >1 yr, much longer than the orbital periods required for a GW merger within a Hubble time. For example, a 40 M_☉ + 40 M_☉ BBH in a circular orbit must have an orbital period <6 days to merge in less than 13.8 Gyr.</p>
- 3. We assume that at the moment the components undergo a PPISN and form a BH they are hydrogen-stripped stars with equal pre-SN masses ($M_{\text{pre SN}}$), leading to an equalmass BBH. This does not imply that the initial mass ratio of the system was unity or that both stars explode simultaneously, but rather that binary interaction happens

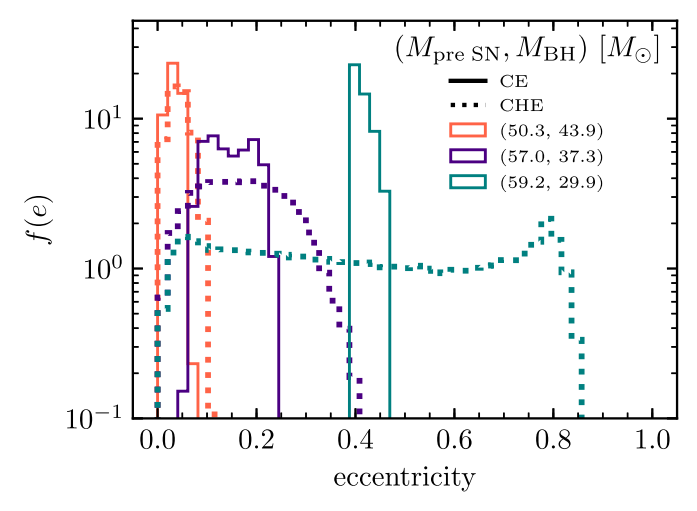


Figure 11. Example distributions of eccentricity enhancements produced by PPISNe in binary systems from CE and CHE evolution. Eccentricities shown correspond to the moment after the formation of the second BH. We consider systems that would result in BBH mergers with a mass ratio of unity, with each color in the diagram indicating the pre-SN mass of the hydrogen-depleted progenitor used and its resulting BH mass.

to produce near-equivalent progenitors. Choosing unequalmass systems leads to higher final eccentricities, so our assumption sets a lower limit on the resulting eccentricities.

Under these assumptions, the initial orbital separation does not play a role in the final eccentricity, and for an individual system one obtains a distribution of eccentricities rather than a unique value.

As in Section 5.1, we assume here that PPISNe do not result in a momentum kick on the resulting remnant. Nevertheless, we have performed simple tests with nonzero kick velocities and found that in general they produce distributions with higher eccentricities. However, for simplicity, we only discuss the case for Blaauw kicks here, so our results serve as a lower limit.

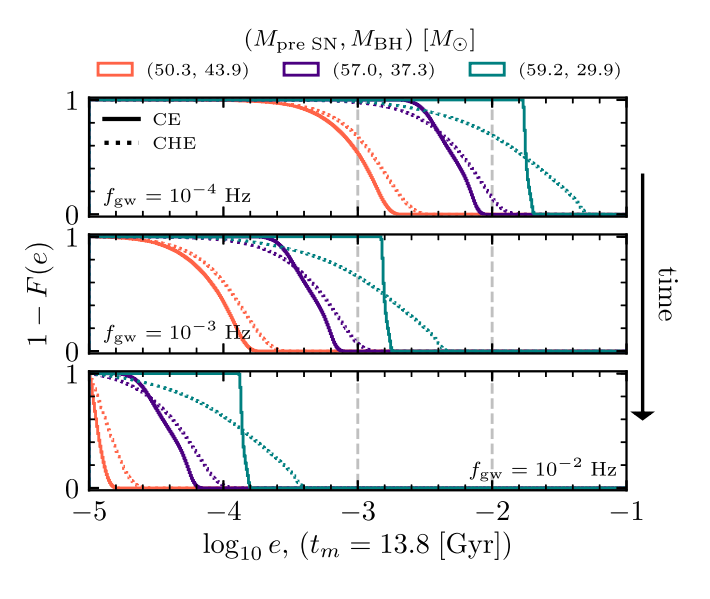
Figure 11 shows the resulting eccentricity distributions for some of our higher mass models, computed using 10⁵ samples for each mass. Lower-mass PPISN progenitors do not lose enough mass to produce eccentricities larger than 0.1. More massive models can actually become unbound as they eject more than half of the total mass in the system (Blaauw 1961), but such extreme systems only happen in a reduced mass range, and we expect them to be uncommon.

After the formation of a BBH, GWs will reduce the orbital period P and the eccentricity of the system. Both quantities then follow a relationship P = P(e), which is independent of the component masses (Peters 1964),

$$P(e) = P_0 \left(\frac{A(e)}{A(e_0)}\right)^{3/2},$$

$$A(e) = \frac{e^{12/19}}{(1 - e^2)} \left(1 + \frac{121}{304}e^2\right)^{870/2299},$$
(6)

where P_0 and e_0 are the initial values. As the orbital period is reduced, the frequency of GW radiation $f_{\rm GW}=2/P$ increases. This means that to translate the birth eccentricities we have computed into eccentricities in the LISA band, we need to specify a birth period as well. As an extreme choice, we set the initial period for each of our simulated binaries such that they have a merger time of $t_m=13.8$ Gyr, and we also consider the



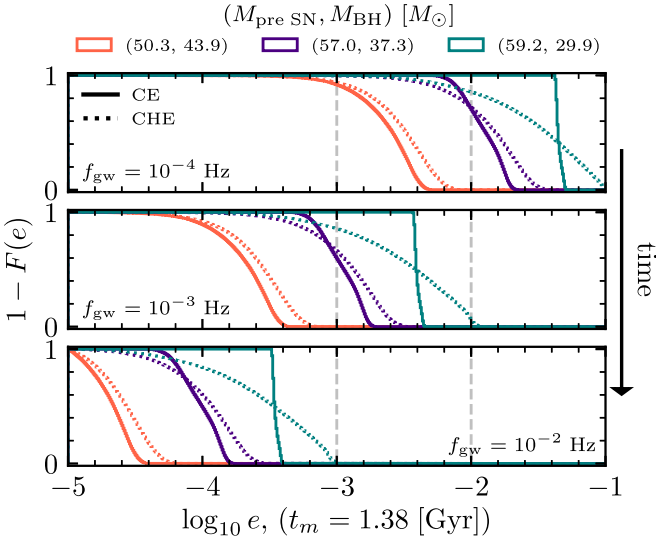


Figure 12. Inverse cumulative distribution functions for eccentricities of different BBH progenitors at frequencies for GW emission relevant to the LISA observatory. As time passes, a BBH is circularized owing to the emission of GWs and emits at higher frequencies. The top panel assumes that the merger time for all sources is $t_m = 13.8$ Gyr, while the bottom panel assumes $t_m = 1.38$ Gyr.

case when $t_m = 1.38 \,\text{Gyr}$ instead. Figure 12 shows how the distributions shown in Figure 11 are changed as a binary evolves owing to GW radiation under these assumptions.

Nishizawa et al. (2016) studied the expected accuracy for eccentricity measurements with the LISA observatory, considering the case of detected BBHs that merge within the mission lifetime $T_{\rm obs}$. For the case of a merger of two $40\,M_\odot$ BHs, this requires the source to be emitting at a frequency larger than 10^{-2} Hz at the beginning of the mission. They showed that eccentricities in excess of e>0.01 would always be measured by LISA, while eccentricities e>0.001 can be measured for 90% (25%) of those mergers considering $T_{\rm obs}=5\,{\rm yr}$ (2 yr). None of our PPISN models reach the peak of sensitivity of LISA ($\sim 10^{-2}\,{\rm Hz}$) with eccentricities above 0.001, so we expect them to be below the threshold for detectability. Thus, we still expect this population to be distinguishable from BBHs predicted to form through dynamical formation.

Note, however, that there is a big caveat to these calculations. As we have shown in Section 4, the systems that we expect to produce measurable eccentricities by LISA are the same ones that would interact strongly in the centuries- to millennia-long phases between pulsations. The calculations done here assume that no circularization due to either tidal interactions or CE evolution happens during this period, something that requires further work to properly assess. As discussed in Section 4.1, for CE phases occurring immediately after the first PPISN pulse, despite the inspiral timescales being short compared to the remaining lifetime of the pulsating star, this does not imply that the orbital separation and eccentricity will be significantly affected by the CE event.

5.3. Impact on Chirp Masses

To study how PPISNe would affect measured chirp masses $(M_{\rm chirp} = [m_1 m_2]^{3/5}/[m_1 + m_2]^{1/5})$ of merging BBHs, we develop a simple model that does not assume any particular formation scenario. Abbott et al. (2016) assume that the more massive BH from a merging BBH follows a Salpeter law $dN/dM_{\rm BH,1} \propto M_{\rm BH,1}^{-\alpha}$ and that the masses of secondaries follow a flat distribution ranging from $M_{\rm min} = 5\,M_\odot$ to $M_{\rm BH,1}$. In a similar way, we assume that the pre-SN mass of one star, $M_{\rm pre~SN,1}$, follows a Salpeter distribution and that its companion mass is distributed flat between $\max(5M_\odot, 0.5M_{\rm pre~SN,1})$ and $M_{\rm pre~SN,1}$. This limits the mass ratio before BH formation to be above 0.5 and is motivated by most formation channels clearly favoring mass ratios closer to unity (see Dominik et al. 2012; Marchant et al. 2016; Rodriguez et al. 2016; Chatterjee et al. 2017).

We randomly sample these distributions, and for each star, if its mass falls below the range for PPISNe of our grid, we assume that it collapses directly to form a BH of mass $M_{\text{pre SN}}$. On the contrary, if it falls above the range of our PPISN models, we assume that it is completely disrupted in a PISN. In the range in between, we interpolate our grid to obtain the final mass of the remnant BH. For α , we choose 2.35, which corresponds to a Salpeter initial mass function (Salpeter 1955). This value of α is consistent with the value inferred by Abbott et al. (2016) using the observed BBHs in the first aLIGO observing run and assuming a power-law distribution. The objective of this experiment is not to provide a definitive prediction but just to illustrate how much of an effect PPISNe can have under simple assumptions on the progenitor population. Note that in this simple approach we do not consider the increase in merger time that would result from ejections. It is not clear whether this would bias observations for or against systems that underwent PPISNe, as longer delay times can lead to mergers at smaller redshifts.

The results of this calculation are shown in Figure 13. For reference, we include a set of calculations where all BHs are assumed to form through direct collapse. Systems that undergo either one or two PPISN events result in lower chirp masses than the model without PPISNe, producing a pileup just below the PISN gap. Moreover, the sensitivity of the aLIGO detectors scales roughly with $M_{\rm BH,1}^{2.2}$ up to total masses of $100\,M_{\odot}$ (Fishbach & Holz 2017). Scaling the distribution of chirp masses we have computed by this factor turns the distribution into a double-peaked one. Future observing runs of the aLIGO/aVirgo detectors are expected to observe tens of merging BBHs in the coming years, constraining the distribution of their chirp masses (Abbott et al. 2016, 2018c). If a clear double-peaked

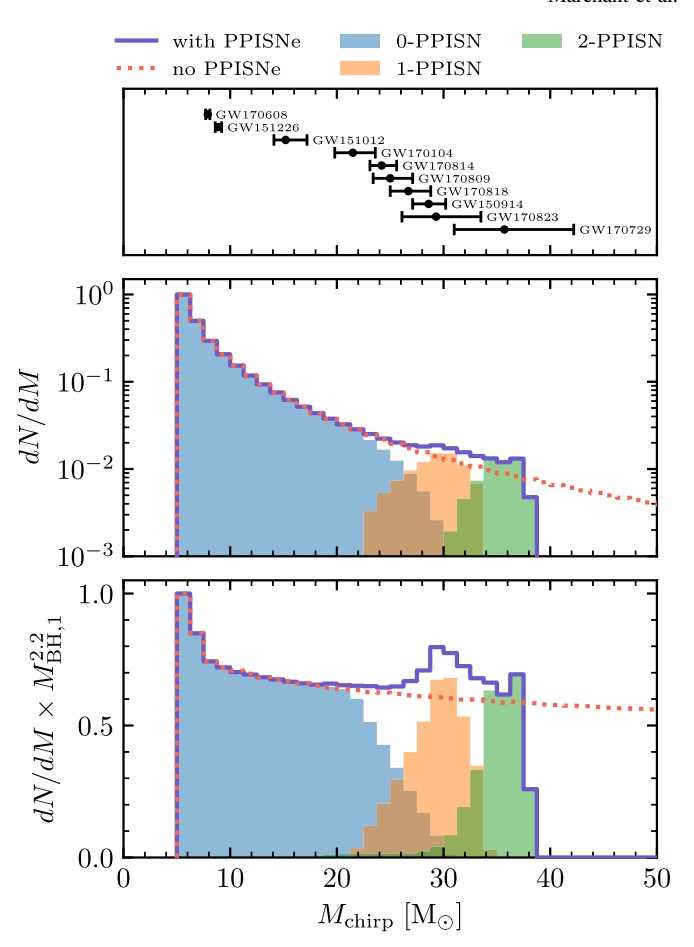


Figure 13. Top: chirp masses of all observed BBH mergers from the first Gravitational Wave Transient Catalog. Middle: distribution of chirp masses in our population synthesis calculation compared to a model with no PPISN. The distribution for models with PPISNe is further separated on the contribution of systems that undergo two, one, or no PPISNe before formation. Bottom: same as before, but scaled by $M_{\rm BH,1}^{2.2}$ to roughly account for the sensitivity dependence with primary mass of the aLIGO/aVirgo detectors.

structure comes out of these measurements, then it should not necessarily be interpreted as two distinct formation channels. Current observations do favor a dearth of BH masses in excess of $45\,M_{\odot}$, but more observations are required to place constraints on the existence of a peak produced by PPISNe (Abbott et al. 2018b).

6. Conclusions

We have shown that PPISNe can lead to strong binary interaction before iron core collapse and BH formation, with systems in orbits compact enough to result in BBH mergers undergoing CE events after the first pulse. Although we do not know the outcome of such CE phases, they can potentially provide interesting electromagnetic counterparts to the PPISN itself. If there is a successful ejection of the CE, this is expected to be observable as a luminous red nova (Ivanova et al. 2013a). Alternatively, the system could fail to eject the CE and result in a merger. If the inspiraling object is a BH, given the large budget of orbital angular momentum in the system, conditions could be appropriate for a long gamma-ray burst in a similar way to the collapsar scenario (Woosley 1993). Even if the CE is ejected, if a few solar masses of material fall back into a BH companion, this can provide sufficient energy to power a hydrogen-poor

superluminous SN (Moriya et al. 2018). Long-lived phases of Roche lobe overflow with a companion BH would lead to the formation of ultraluminous X-ray sources (see Kaaret et al. 2017 for a recent review), with peculiar CO giants or supergiants as donors. Most of these potential outcomes are speculative at this point but merit detailed further study potentially through the use of 3D hydrodynamical simulations.

We have also shown that PPISNe can modify various observable properties of merging BBHs, including their spins, eccentricities, and chirp masses. However, to do so, we have ignored the potential interaction of a star undergoing a PPISN with its companion. Properly characterizing these interaction phases is then fundamental to understanding how stars that undergo PPISNe contribute to the overall population of merging BBHs.

P.M. would like to thank Francis Timmes, Giacomo Terreran, Takashi Moriya, and Christopher Berry for useful discussions. P.M. acknowledges support from NSF grant AST-1517753. S.d.M. and M.R. acknowledge funding by the European Union's Horizon 2020 research and innovation program from the European Research Council (ERC) (grant agreement No. 715063) and by the Netherlands Organisation for Scientific Research (NWO) as part of the Vidi research program BinWaves with project No. 639.042.728. R.F. is supported by an NWO top grant with project No. 614.001.501. V.K. is a CIFAR Research Fellow, and V.K. and K.P. acknowledge support by the CIFAR program in Gravity and Extreme Universe. P.M. also thanks the Kavli Institute for theoretical physics of the university of California Santa Barbara, together with the participants of the "Astrophysics from LIGO's First Black Holes" and "The Mysteries and Inner Workings of Massive Stars" programs for helpful discussion. For this project the SAO/NASA Astrophysics Data System (ADS) was used extensively.

Software: MESA (Paxton et al. 2011, 2013, 2015, 2018, mesa.sourceforge.net), Python available from https://www.python.org, matplotlib (Hunter 2007), NumPy (van der Walt et al. 2011), ipython/jupyter (Pérez & Granger 2007; Kluyver et al. 2016), inkscape available from https://inkscape.org/.

Appendix A Time-dependent Convection

During phases of dynamical instability, large regions in the star can switch back and forth between being stable or unstable to convection on timescales comparable to or shorter than a convective turnover timescale. To properly treat energy transport under these conditions, a model for time-dependent convection is required. Here we describe a simple model that captures the relevant timescales and reduces to standard mixing-length theory (MLT; Böhm-Vitense 1958) in long timescales. We follow the work of Arnett (1969) and consider the average convective velocity v_c in MLT to be an independent variable that satisfies the equation

$$\frac{\partial v_c}{\partial t} = \frac{v_{\text{MLT}}^2 - v_c^2}{\lambda}, \quad \text{for convectively unstable regions,} \quad (7)$$

where $v_{\rm MLT}$ is the steady-state value predicted by MLT. λ is the mixing length, which we define as $\alpha_{\rm MLT}H_P$, where $\alpha_{\rm MLT}$ is a free parameter of order unity and H_P is the local pressure scale height. In particular, for our simulations we use $\alpha_{\rm MLT}=2$. On timescales much longer than a convective turnover timescale

 $(au_{
m to} = \lambda/v_{
m MLT})$ convective velocities asymptotically approach the steady-state value $v_{
m MLT}$, recovering standard MLT. In regions that are convectively stable $v_{
m MLT} = 0$, and simply using Equation (7) would result in convective velocities decaying on a timescale $au = \lambda/v_c$, which becomes infinitely large as convective velocities are reduced. This ignores the actual timescale in which fluid parcels would be slowed down in a stratified medium. To provide an order-of-magnitude correction to this, we construct a timescale $au_N = 1/N$, where N is the Brunt–Väisällä frequency, and use

$$\frac{\partial v_c}{\partial t} = -\frac{v_c^2}{\lambda} - \frac{v_c}{\tau_N}, \quad \text{for convectively stable regions} \quad (8)$$

to model the shutoff of convection. Mixing from convection is modeled as a diffusive process with a diffusion coefficient $D = v_c \lambda/3$.

In its standard form, MLT solves an algebraic system of three equations to compute the steady-state convective velocity v_{MLT} , the temperature gradient of the star ∇ , and the temperature gradient of displaced blobs of material ∇' , which differs from the adiabatic gradient ∇_a due to radiative energy losses. In our case, we require a derivation of MLT for a given value of v_c rather than the steady-state one. Following Cox & Giuli (1968), if convective velocities are given, then the convective efficiency Γ (which is the ratio of energy radiated by a moving parcel to the energy released when it dissolves after crossing a mixing length) can be directly computed as

$$\Gamma = \frac{c_P}{6ac} \frac{\kappa \rho^2 v_c \lambda}{T^3}.$$
 (9)

Using this, the values of ∇ and ∇' can be determined from

$$\nabla_{r} = \nabla - \frac{9}{4}\Gamma(\nabla - \nabla'),$$

$$\frac{\nabla_{r} - \nabla}{\nabla_{r} - \nabla_{r}} = \frac{9\Gamma^{2}/4}{1 + \Gamma(1 + 9\Gamma/4)},$$
(10)

where ∇_r is the radiative temperature gradient. All of these are standard results of MLT (see Cox & Giuli 1968), but we have taken care here to only use expressions that do not assume a steady-state value for v_c in order to have a self-consistent model. Although this model incorporates the timescales relevant to the process, it does not intend to solve some of the long-standing problems with MLT (see Arnett et al. 2018 for a recent discussion). For instance, our model does not incorporate overshooting directly but instead uses an exponentially decaying mixing coefficient beyond convective regions (see Section 2) that does not account for energy transport. Also, sharp composition gradients near convective boundaries can lead to discontinuities in the Brunt–Väisälä frequency, producing a discontinuous $\partial v_c/\partial t$ and v_c at a convective boundary. Under these circumstances, we would expect turbulent energy to be transported through the boundary, but our model does not include this effect.

Appendix B Resolution and Nuclear Reaction Network Convergence Test

In order to test whether our results are converged, we have performed a test using the first pulse of our $84\,M_\odot$ model.

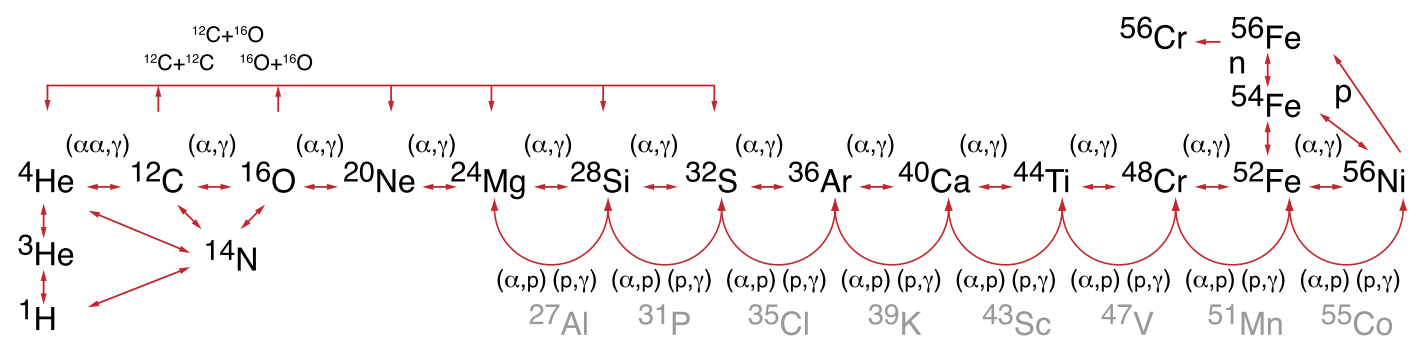


Figure 14. List of isotopes and linkages in the approx21 network used during late burning stages in our calculations.

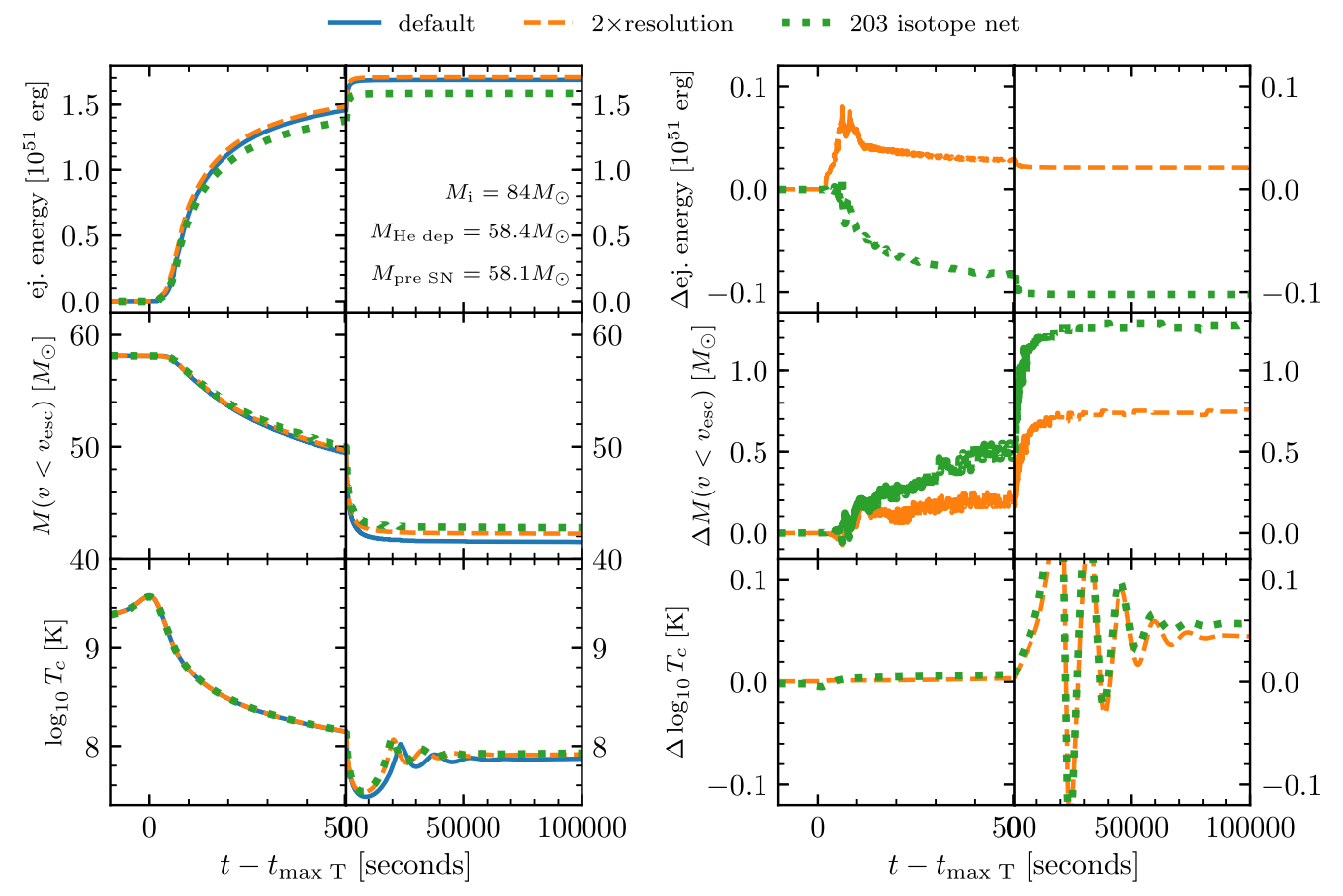


Figure 15. Left: evolution of the kinetic energy of ejected layers, the mass at velocities below the escape velocity, and central temperature for the first pulse of an $M_i = 84 M_{\odot}$ progenitor. Results are shown for the default set of parameters used in this paper, a simulation with double the resolution in time and space, and one with a 203-isotope network rather than the default 21-isotope network we use for all other models. Right: for the simulations with higher resolution and a bigger network, each line shows how the difference with respect to the simulation with our default choice of parameters evolves with time.

Using our default setup, at the onset of the pulse this star has $58.1\,M_\odot$, and after the first mass ejection it ends up with a mass of $41.49\,M_\odot$. During this phase, the model is resolved using between $\sim\!2500$ and 3500 cells and $\sim\!6000$ time steps. To test the convergence of our model to changes in spatial and temporal resolution, we have computed a model that after helium depletion approximately doubles both.

During the pulsational phase, we use the approx21 reaction network, for which the isotopes and linkages are shown in Figure 14. The backbone is a strict α -chain composed of (α, γ) and (γ, α) links among the 13 isotopes ⁴He, ¹²C, ¹⁶O, ²⁰Ne, ²⁴Mg, ²⁸Si, ³²S, ³⁶Ar, ⁴⁰Ca, ⁴⁴Ti, ⁴⁸Cr, ⁵²Fe, and ⁵⁶Ni. Above

 $\simeq 2.5 \times 10^9$ K it is essential to include $(\alpha, p)(p, \gamma)$ and $(\gamma, p)(p, \alpha)$ links in order to obtain reasonably accurate energy generation rates and abundances (Timmes et al. 2000). At these elevated temperatures the flows through the $(\alpha, p)(p, \gamma)$ sequences are faster than the flows through the (α, γ) channels. An $(\alpha, p)(p, \gamma)$ sequence is, effectively, an (α, γ) reaction through an intermediate isotope. Approx21 includes eight $(\alpha, p)(p, \gamma)$ sequences and their inverses by assuming steady-state proton flows through the intermediate isotopes 27 Al, 31 P, 35 Cl, 39 K, 43 Sc, 47 V, 51 Mn, and 55 Co. The assumed steady-state proton flows allow inclusion of the $(\alpha, p)(p, \gamma)$ sequences without explicitly evolving the proton or intermediate isotope

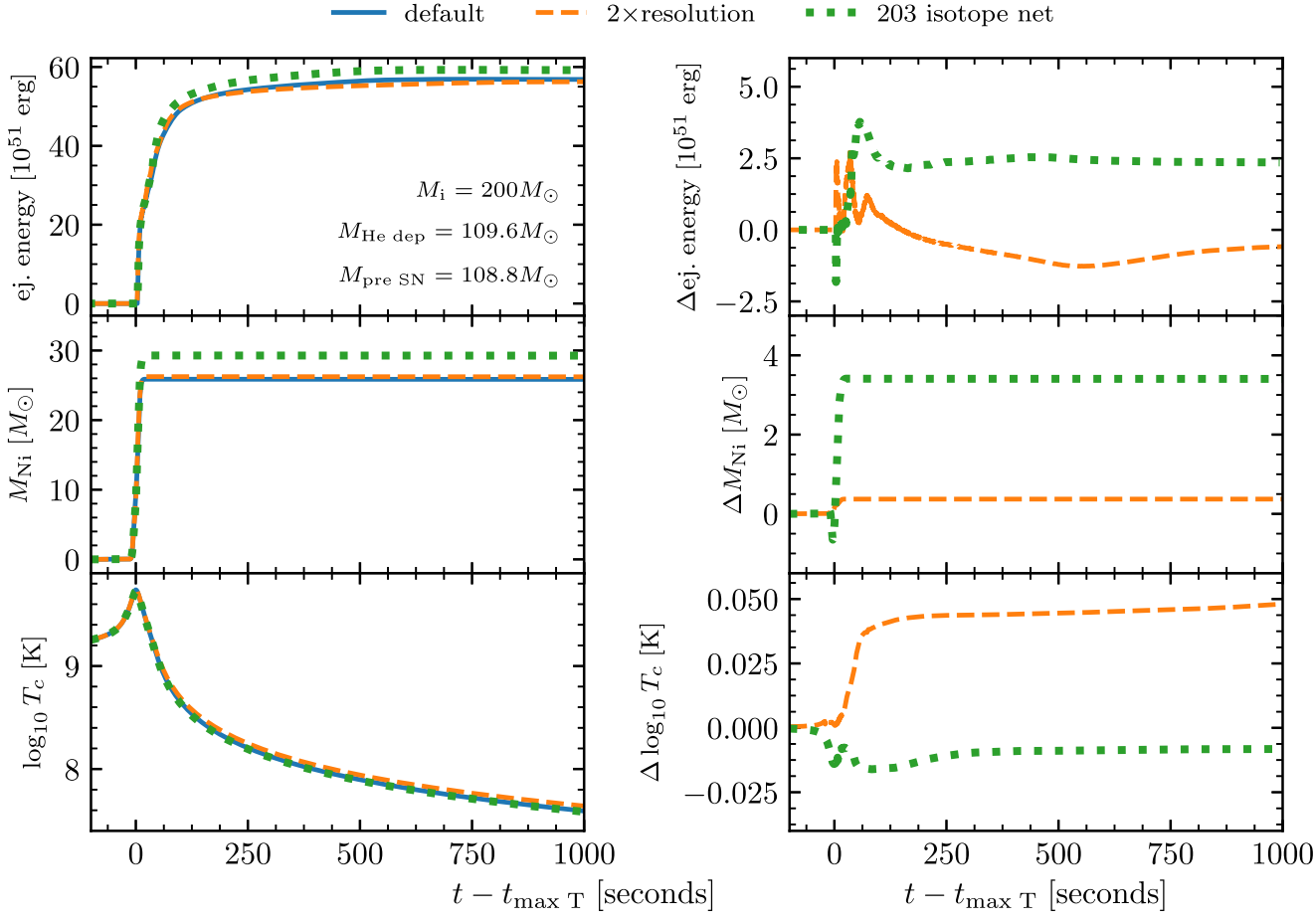


Figure 16. Same as Figure 15, but for a PISN model with $M_i = 200 M_{\odot}$ ($M_{\text{pre SN}} = 108.4 M_{\odot}$), and showing the evolution of the total mass of ⁵⁶Ni instead of the ejected mass.

abundances. In addition to this α -chain backbone, approx21 includes approximations for steady-state hydrogen burning (PP chain and CNO cycle), carbon and oxygen burning ($^{12}\text{C} + ^{12}\text{C}$, $^{12}\text{C} + ^{16}\text{O}$, $^{16}\text{O} + ^{16}\text{O}$), and aspects of photodisintegration with ^{54}Fe . These additions are briefly described in Weaver et al. (1978). Finally, approx21 adds the ^{56}Cr and ^{56}Fe isotopes and tuned steady-state reaction sequences to attain a reasonably accurate lower electron fraction Y_e (as compared to much larger reaction networks) for pre-SN models (Paxton et al. 2015). To test the accuracy of this few-isotope network during a pulse, we have also computed the first pulse of our $84\,M_\odot$ model using the 203-isotope network of Renzo et al. (2017), which is tuned to properly capture silicon burning.

Figure 15 shows the results of our convergence tests. For ease of comparison between the simulations, we have matched all tracks in time to the point where the first pulsation reaches its maximum central temperature, and we compare values $100,000\,\mathrm{s}$ after this point. Overall the three simulations are quantitatively consistent, with relative differences in the kinetic energy of ejected layers and final masses of around 6%. Final central temperatures digress by around 15%, but considering that during the pulse it is lowered by a factor of ~ 30 , this is a small error. Given these results, and that we do not study detailed nucleosynthetic yields of PPISNe or PISNe in this work, we consider our choice of resolution and nuclear reaction network appropriate. In particular, the use of approx21 instead of the 203-isotope network reduces the runtime of each model

by more than a factor of 10, significantly lowering the cost of our simulations.

As a more extreme example, we repeat this exercise for a PISN model with an initial mass of $M_i = 200 M_{\odot}$, which is shown in Figure 16. This model is near the upper end of the mass range of PISNe, with $M_{\text{pre SN}} = 108.4$, and during the explosion it reaches a central temperature of 5.2×10^9 K, significantly higher than the first pulse of the PPISN model shown before, which reaches a maximum temperature of 3.2×10^9 K. The model with the approx21 network produces a total of $25.9 \, M_{\odot}$ of 56 Ni, which is $\sim 13\%$ lower than that produced by the model with the 203-isotope network. The error on the kinetic energy of the ejecta is similar to that of the PPISN model, with the 203-isotope network predicting an ejecta energy \sim 4% larger than that of the approx21 model. We see that the dynamics of the explosion are consistently reproduced, although the difference in nickel mass would produce nonnegligible differences on the resulting light curves. Our focus, however, is on the evolution of PPISNe, which do not produce significant amounts of nickel, so we still consider the use of approx21 to be justified.

Appendix C Precision of the Relaxation Procedure

To model the long-lived phases between pulses in our more massive progenitors, we use a relaxation procedure that creates a hydrostatic model from scratch that matches the mass,

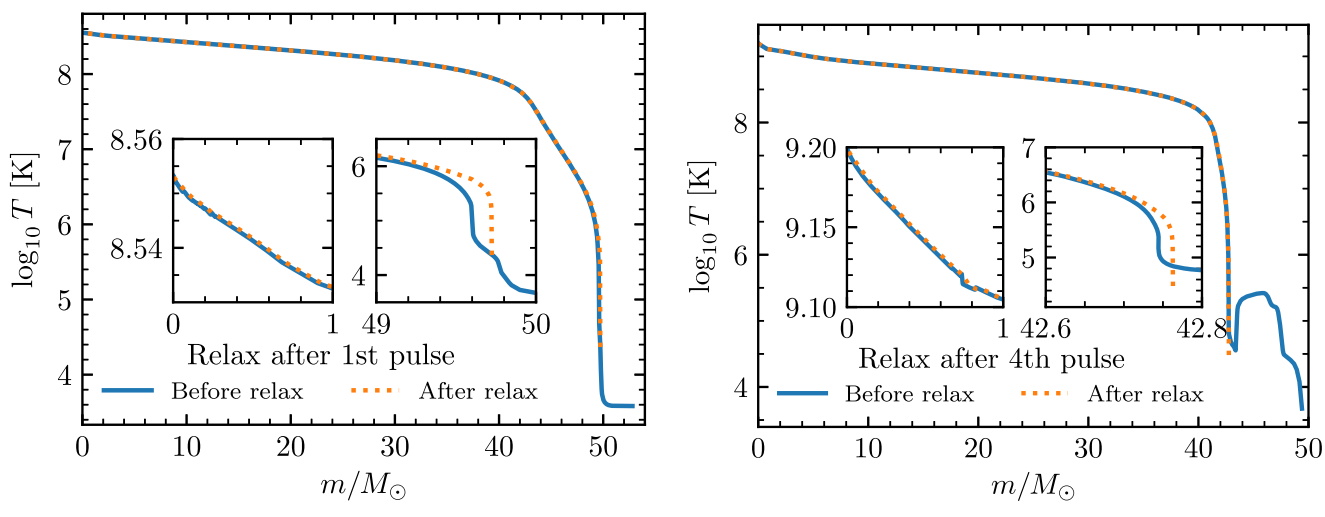


Figure 17. Pre- and post-relaxation temperature profiles for our $M_i = 76 M_{\odot}$ model after the first and fourth pulses.

entropy, and composition profile after the pulse. This method has been described in Appendix B of Paxton et al. (2018), and here we show how well it reproduces the pre-relaxation model. In order to perform a relaxation after a pulse, we require that velocities are below $20\,\mathrm{km\,s^{-1}}$ and no layers are moving at more than 50% their local sound speed within the inner 99% of mass that remains bound. To prevent the relaxation happening when these thresholds are satisfied during minima and maxima of oscillations, we require these to be satisfied for at least 100 continuous time steps. We also require the neutrino and nuclear burning luminosities to be below 10^{11} and $10^{10}\,L_\odot$ respectively, in order to avoid relaxing the model when the core is evolving on a timescale of \sim days.

Figure 17 shows the outcome of two relaxation procedures done for the $76 M_{\odot}$ model shown in Figure 2 after the first and fourth pulses. For the other three pulses shown, the conditions on the luminosities are not satisfied, so the model is evolved further without removing the outer layers. As can be seen, except for the very outermost layers temperatures are matched very accurately in the relaxed model, with the central temperature differing by 0.0002 and 0.0005 dex for the first and fourth pulse, respectively. As expected, the very outermost layers show more noticeable differences, with clear digressions being visible at the outer ~ 0.2 and $\sim 0.05 M_{\odot}$ after the first and fourth pulse, respectively. Although a difference is expected, since the very outermost layers are still falling back when the relaxation is made, we do care about accurately characterizing observable properties of the star in between pulses. However, the discrepancy turns out to be not very important. After the first pulse, the thermal timescale of the outer $0.2 M_{\odot}$ is just 1.4 yr, a very small time compared to the almost three millennia between the first and second pulse. This means that although we do not trust the effective temperature and luminosity of our models immediately after a pulse, after ~ 1 yr any anomalies from relaxation in the outermost layers will be removed.

ORCID iDs

Ronald E. Taam https://orcid.org/0000-0001-8805-2865

Selma E. de Mink https://orcid.org/0000-0001-9336-2825 Vassiliki Kalogera https://orcid.org/0000-0001-9236-5469

References

```
Abbott, B. P., Abbott, R., Abbott, T. D., et al. 2016, PhRvX, 6, 041015
Abbott, B. P., Abbott, R., Abbott, T. D., et al. 2018a, arXiv:1811.12907
Abbott, B. P., Abbott, R., Abbott, T. D., et al. 2018b, arXiv:1811.12940
Abbott, B. P., Abbott, R., Abbott, T. D., et al. 2018c, LRR, 21, 3
Abell, P. A., Allison, J., Anderson, S. F., et al. 2009, arXiv:0912.0201
Ade, P. A. R., Aghanim, N., Arnaud, M., et al. 2016, A&A, 594, A13
Angulo, C., Arnould, M., Rayet, M., et al. 1999, NuPhA, 656, 3
Antonini, F., Murray, N., & Mikkola, S. 2014, ApJ, 781, 45
Antonini, F., Toonen, S., & Hamers, A. S. 2017, ApJ, 841, 77
Arcavi, I., Howell, D. A., Kasen, D., et al. 2017, Natur, 551, 210
Arnett, W. D. 1969, Ap&SS, 5, 180
Arnett, W. D., Meakin, C., Hirschi, R., et al. 2018, arXiv:1810.04653
Asplund, M., Grevesse, N., Sauval, A. J., & Scott, P. 2009, ARA&A, 47, 481
Bartos, I., Kocsis, B., Haiman, Z., & Márka, S. 2017, ApJ, 835, 165
Belczynski, K., Buonanno, A., Cantiello, M., et al. 2014, ApJ, 789, 120
Belczynski, K., Heger, A., Gladysz, W., et al. 2016a, A&A, 594, A97
Belczynski, K., Holz, D. E., Bulik, T., & O'Shaughnessy, R. 2016b, Natur,
  534, 512
Bellm, E. 2014, in The Third Hot-wiring the Transient Universe Workshop, ed.
  P. R. Wozniak (Stanford, CA: Stanford Univ. Press), 27
Blaauw, A. 1961, BAN, 15, 265
Boersma, J. 1961, BAN, 15, 291
Böhm-Vitense, E. 1958, ZA, 46, 108
Bond, J. R., Arnett, W. D., & Carr, B. J. 1982, in NATO Advanced Science
  Institutes (ASI) Series C, Vol. 90, ed. M. J. Rees & R. J. Stoneham
  (Dordrecht: Reidel), 303
Breivik, K., Rodriguez, C. L., Larson, S. L., Kalogera, V., & Rasio, F. A. 2016,
   ApJL, 830, L18
Brott, I., de Mink, S. E., Cantiello, M., et al. 2011, A&A, 530, A115
Caughlan, G. R., & Fowler, W. A. 1988, ADNDT, 40, 283
Chan, C., Müller, B., Heger, A., Pakmor, R., & Springel, V. 2018, ApJL,
  852, L19
Chatterjee, S., Rodriguez, C. L., & Rasio, F. A. 2017, ApJ, 834, 68
Chatzopoulos, E., & Wheeler, J. C. 2012, ApJ, 748, 42
Chatzopoulos, E., Wheeler, J. C., & Couch, S. M. 2013, ApJ, 776, 129
Chen, K.-J., Woosley, S., Heger, A., Almgren, A., & Whalen, D. J. 2014, ApJ,
Clark, J. P. A., van den Heuvel, E. P. J., & Sutantyo, W. 1979, A&A, 72, 120
Cox, J. P., & Giuli, R. T. 1968, Principles of Stellar Structure (London: Gordon
  and Breach)
de Mink, S. E., & Mandel, I. 2016, MNRAS, 460, 3545
Dominik, M., Belczynski, K., Fryer, C., et al. 2012, ApJ, 759, 52
Fishbach, M., & Holz, D. E. 2017, ApJL, 851, L25
Fowler, W. A., & Hoyle, F. 1964, ApJS, 9, 201
Fraley, G. S. 1968, Ap&SS, 2, 96
Fryer, C. L. 1999, ApJ, 522, 413
```

Gal-Yam, A., Mazzali, P., Ofek, E. O., et al. 2009, Natur, 462, 624

```
Glatzel, W., Fricke, K. J., & El Eid, M. F. 1985, A&A, 149, 413
Hamann, W.-R., Koesterke, L., & Wessolowski, U. 1995, A&A, 299, 151
Hannam, M., Brown, D. A., Fairhurst, S., Fryer, C. L., & Harry, I. W. 2013,
   ApJL, 766, L14
Heger, A., Langer, N., & Woosley, S. E. 2000, ApJ, 528, 368
Heger, A., & Woosley, S. E. 2002, ApJ, 567, 532
Heger, A., Woosley, S. E., & Spruit, H. C. 2005, ApJ, 626, 350
Herwig, F. 2000, A&A, 360, 952
Hulse, R. A., & Taylor, J. H. 1975, ApJL, 195, L51
Hunter, J. D. 2007, CSE, 9, 90
Iglesias, C. A., & Rogers, F. J. 1996, ApJ, 464, 943
Ivanova, N., Justham, S., Avendano Nandez, J. L., & Lombardi, J. C. 2013a,
    ci, 339, 433
Ivanova, N., Justham, S., Chen, X., et al. 2013b, A&ARv, 21, 59
Kaaret, P., Feng, H., & Roberts, T. P. 2017, ARA&A, 55, 303
Kluyver, T., Ragan-Kelley, B., Pérez, F., et al. 2016, in Proc. 20th Int. Conf. on
   Electronic Publishing, Positioning and Power in Academic Publishing: Players,
   Agents and Agendas, ed. F. Loizides & B. Schmidt (Amsterdam: IOS Press)
Kulkarni, S. R., Hut, P., & McMillan, S. 1993, Natur, 364, 421
Kuroda, T., Kotake, K., Takiwaki, T., & Thielemann, F.-K. 2018, MNRAS,
   477, L80
Langer, N., Fricke, K. J., & Sugimoto, D. 1983, A&A, 126, 207
Lipunov, V. M., Postnov, K. A., & Prokhorov, M. E. 1997, NewA, 2, 43
Lunnan, R., Fransson, C., Vreeswijk, P. M., et al. 2018, NatAs, 2, 887
Maeder, A. 1987, A&A, 178, 159
Mandel, I., & de Mink, S. E. 2016, MNRAS, 458, 2634
Marchant, P., Langer, N., Podsiadlowski, P., Tauris, T. M., & Moriya, T. J.
   2016, A&A, 588, A50
Mokiem, M. R., de Koter, A., Vink, J. S., et al. 2007, A&A, 473, 603
Moriya, T. J., Nicholl, M., & Guillochon, J. 2018, ApJ, 867, 113
Nieuwenhuijzen, H., & de Jager, C. 1990, A&A, 231, 134
Nishizawa, A., Berti, E., Klein, A., & Sesana, A. 2016, PhRvD, 94, 064020
Ott, C. D., Roberts, L. F., da Silva Schneider, A., et al. 2018, ApJL, 855, L3
Paczynski, B. 1976, in IAU Symp. 73, Structure and Evolution of Close Binary
   Systems, ed. P. Eggleton, S. Mitton, & J. Whelan (Dordrecht: Reidel), 75
Paxton, B., Bildsten, L., Dotter, A., et al. 2011, ApJS, 192, 3
Paxton, B., Cantiello, M., Arras, P., et al. 2013, ApJS, 208, 4
Paxton, B., Marchant, P., Schwab, J., et al. 2015, ApJS, 220, 15
```

```
Paxton, B., Schwab, J., Bauer, E. B., et al. 2018, ApJS, 234, 34
Pérez, F., & Granger, B. E. 2007, CSE, 9, 21
Peters, P. C. 1964, PhRv, 136, 1224
Portegies Zwart, S. F., & McMillan, S. L. W. 2000, ApJL, 528, L17
Rakavy, G., & Shaviv, G. 1967, ApJ, 148, 803
Renzo, M., Ott, C. D., Shore, S. N., & de Mink, S. E. 2017, A&A, 603, A118
Rodriguez, C. L., Chatterjee, S., & Rasio, F. A. 2016, PhRvD, 93, 084029
Salpeter, E. E. 1955, ApJ, 121, 161
Sesana, A. 2016, PhRvL, 116, 231102
Sigurdsson, S., & Hernquist, L. 1993, Natur, 364, 423
Smith, R. M., Dekany, R. G., Bebek, C., et al. 2014, Proc. SPIE, 9147, 914779
Soberman, G. E., Phinney, E. S., & van den Heuvel, E. P. J. 1997, A&A,
Spera, M., & Mapelli, M. 2017, MNRAS, 470, 4739
Stone, N. C., Metzger, B. D., & Haiman, Z. 2017, MNRAS, 464, 946
Stothers, R. B. 1999, MNRAS, 305, 365
Taam, R. E., Bodenheimer, P., & Ostriker, J. P. 1978, ApJ, 222, 269
Takahashi, K. 2018, ApJ, 863, 153
Terreran, G., Pumo, M. L., Chen, T.-W., et al. 2017, NatAs, 1, 713
Thompson, T. A. 2011, ApJ, 741, 82
Timmes, F. X., Hoffman, R. D., & Woosley, S. E. 2000, ApJS, 129, 377
Toro, E. F., Spruce, M., & Speares, W. 1994, ShWav, 4, 25
Tutukov, A. V., & Yungelson, L. R. 1993, MNRAS, 260, 675
van den Heuvel, E. P. J. 1976, in IAU Symp. 73, Structure and Evolution of
  Close Binary Systems, ed. P. Eggleton, S. Mitton, & J. Whelan (Dordrecht:
  Reidel), 35
van der Walt, S., Colbert, S. C., & Varoquaux, G. 2011, CSE, 13, 22
Vink, J. S., de Koter, A., & Lamers, H. J. G. L. M. 2001, A&A, 369, 574
Weaver, T. A., Zimmerman, G. B., & Woosley, S. E. 1978, ApJ, 225, 1021
Woosley, S. E. 1993, ApJ, 405, 273
Woosley, S. E. 2017, ApJ, 836, 244
Woosley, S. E. 2018, ApJ, 863, 105
Woosley, S. E., Blinnikov, S., & Heger, A. 2007, Natur, 450, 390
Woosley, S. E., & Weaver, T. A. 1982, in NATO Advanced Science Institutes
  (ASI) Series C, Vol. 90, ed. M. J. Rees & R. J. Stoneham (Dordrecht:
  Reidel), 79
Yoon, S.-C., Woosley, S. E., & Langer, N. 2010, ApJ, 725, 940
Yoshida, T., Umeda, H., Maeda, K., & Ishii, T. 2016, MNRAS, 457, 351
```